

# Carbon in the N159/N160 Complex of the Large Magellanic Cloud

Alberto D. Bolatto<sup>1</sup>, James M. Jackson<sup>2</sup>,

Institute for Astrophysical Research, Department of Astronomy  
Boston University, 725 Commonwealth Ave., Boston MA 02215

Frank P. Israel<sup>3</sup>,

Sterrewacht Leiden, P.O. Box 9513, NL 2300-RA Leiden, The Netherlands

Xiaolei Zhang<sup>4</sup>

Smithsonian Astrophysical Observatory, 60 Garden St. MS 78, Cambridge, MA 02138

and

Sungeun Kim<sup>5</sup>

University of Illinois at Urbana-Champaign, Department of Astronomy, 1002 West Green  
St., Urbana, IL 61801

## ABSTRACT

We present a study of carbon in N159/N160, an H II region complex in the low metallicity Large Magellanic Cloud. We have mapped this region, which comprises four distinct molecular clouds spanning a wide range of star-formation activity, in four transitions:  $^{13}\text{CO}$  ( $J = 1 \rightarrow 0$ ),  $^{12}\text{CO}$  ( $J = 2 \rightarrow 1$ ) and ( $J = 4 \rightarrow 3$ ), and [C I] ( ${}^3\text{P}_1 \rightarrow {}^3\text{P}_0$ ). Combining these data with existing [C II] ( ${}^2\text{P}_{3/2} \rightarrow {}^2\text{P}_{1/2}$ ) observations provides a complete picture of the predominant forms of carbon in the gas phase of the ISM. The new CO ( $J = 2 \rightarrow 1$ ) data show that the complex is immersed in an envelope of extended, low level emission, undetected by previous ( $J = 1 \rightarrow 0$ ) mapping efforts. The  $^{12}\text{CO}$

---

<sup>1</sup>bolatto@bu.edu

<sup>2</sup>jackson@bu-ast.bu.edu

<sup>3</sup>israel@strw.leidenuniv.nl

<sup>4</sup>Currently at Raytheon ITSS and NASA GSFC, code 685, Greenbelt, MD 20771  
(xzhang@spec1.gsfc.nasa.gov)

<sup>5</sup>Currently at Smithsonian Astrophysical Observatory (skim@cfa.harvard.edu)

$(J = 2 \rightarrow 1)/(J = 1 \rightarrow 0)$  ratio in this envelope is  $\gtrsim 3$ , a value consistent with optically thin CO emission. The envelope is also relatively bright in [C I] and [C II], and calculations show that it is mostly photodissociated: it appears to be translucent ( $A_V < 1$ ). Neutral carbon emission in the complex unexpectedly peaks at the quiescent southern cloud (N159S). In the northern portion of the map (the N160 nebula), the H II regions prominent in [C II] correspond to holes in the [C I] distribution. Overall we find that, while the  $I_{[CII]}/I_{CO}$  ratio is enhanced with respect to similar complexes in the Milky Way, the  $I_{[CI]}/I_{CO}$  ratio appears to be similar or reduced.

*Subject headings:* Magellanic Clouds — galaxies: ISM — galaxies: irregular — radio lines: ISM — submillimeter — ISM: clouds

## 1. Introduction

The Magellanic Clouds are especially interesting systems for the study of the interstellar medium (ISM). Their low heavy element abundances and low dust-to-gas ratios, coupled with their proximity and their active star formation, make them ideal laboratories for understanding how metallicity and strong radiation fields influence the composition and structure of the ISM. Furthermore, in several important aspects they resemble primeval galaxies: they are morphologically irregular, metal-poor, and very actively forming massive stars. It is, however, worthwhile to point out that the Magellanic Clouds are not pristine systems. Their irregular morphologies refer mostly to the young populations (massive stars, OB associations, and H II regions), probably influenced by recent encounters with the Milky Way: the distribution of old stars and overall mass is not irregular (Cioni, Habing & Israel 2000). Nevertheless, because of a relatively low time-averaged star formation rate the Magellanic Clouds are considerably less developed than the Milky Way. Therefore their study will advance the understanding of the interaction between star formation and the ISM in primordial systems.

The H II regions in the N159/N160 complex were first cataloged by Henize (1956) in a survey of emission line nebulae in the Large Magellanic Cloud (Davies, Elliot, & Meaburn 1976 give them the numbers 271 and 284). These nebulae are two of the brightest H II regions in the immediate vicinity of 30 Doradus, located  $\sim 40'$  to its south.

In this region the star formation activity appears to be progressing from the (relatively) evolved starburst of 30 Doradus, where most of the enshrouding molecular cloud has been dissipated (Johansson et al. 1998), towards the quiescent southern CO arm region where

little or no star formation is currently taking place (Cohen et al. 1988; Kutner et al. 1997). Located at such a transitional place the N159/N160 complex is one of the best studied star-forming regions of the Large Magellanic Cloud in molecular and atomic transitions (e.g., Johansson et al. 1994; Israel et al. 1996; Stark et al. 1997a; Pak et al. 1998; Johansson et al. 1998; Heikkilä, Johansson, & Olofsson 1999).

The N159/N160 complex features three distinct and spatially well separated regions: 1) the northern region, chiefly associated with the N160 nebula, where massive star formation is well evolved and the parent clouds have been mostly, albeit not completely, photodissociated and dissipated. 2) The central region, associated with the N159 nebula, which is undergoing strong star formation activity but still wrapped in molecular gas. This region includes two giant molecular clouds (GMCs) known as N159-east and N159-west (N159E and N159W respectively). And, 3) the southern region, featuring the molecular cloud N159-south (N159S). This cloud is actually the beginning of the 30 Doradus CO ridge region, a  $\sim 900$  pc ( $\sim 1^\circ$ ) long spur of molecular material extending southward of the 30 Doradus nebula.

The 30 Doradus CO ridge is the largest concentration of CO in the LMC (Cohen et al. 1988). Because the ridge is located on the leading edge of the LMC's movement through the hot Galactic halo (Mathewson & Ford 1984), its formation has been attributed to ram pressure compression of the Magellanic interstellar medium (de Boer et al. 1998; Kim et al. 1998). The entire ridge region (including N159S) is quiescent, with little or no star formation activity as evidenced by its faint far-infrared (FIR), H $\alpha$  (Davies et al. 1976), and [C II] emission (Mochizuki et al. 1994).

Because dust is the dominant source of UV extinction, the low dust-to-gas ratio of the metal-poor ISM allows the UV radiation to penetrate more deeply into the molecular material thereby causing widespread photodissociation and photoionization. The regions, at the surfaces of clouds, where the UV radiation dominates the heating and chemistry of the ISM are known as photon-dominated or photodissociation regions (PDRs). In these regions the UV radiation dissociates most molecular species, but leaves H<sub>2</sub> relatively intact because of its strong self-shielding (Abgrall et al. 1992; Pak et al. 1998). Therefore in metal-poor systems an increasingly large fraction of the molecular gas is expected to be associated with C<sup>0</sup> and C<sup>+</sup>, rather than CO. Observations of CO together with its photodissociation and photoionization products (C<sup>0</sup> and C<sup>+</sup>) are the key to understand the interplay between the radiation field and the chemical and physical structure of molecular clouds in low metallicity systems (e.g., Bolatto, Jackson, & Ingalls 1999; Bolatto et al. 2000). This paper presents some of these observations.

What is the dust-to-gas ratio in the LMC and how does it affect its PDRs? Several

arguments suggest that the dust-to-gas ratio of a galaxy is proportional to its metallicity  $Z$  (Franco & Cox 1986), but recent studies find a  $Z^2$  dependence (Lisenfeld & Ferrara 1998). Independently of this, the dust-to-gas ratios measured in the Magellanic Clouds are  $\sim 1/4$  and  $\sim 1/8$  of the Galactic value (LMC and SMC respectively, Koornneef 1982; Bouchet et al. 1985), while their metallicities (measured through the oxygen abundance) are  $Z_{\text{LMC}} \sim Z_{\text{Orion}}/2$  and  $Z_{\text{SMC}} \sim Z_{\text{Orion}}/5$ . Because of this relative lack of dust, to achieve the same visual extinction  $A_V$  in the LMC requires  $\sim 4$  times larger gas columns than in the Milky Way. Therefore, PDRs are expected to be on average  $\sim 4$  times more extended in the LMC, while the CO cores will be 4 times smaller (e.g., Israel 1997; Pak et al. 1998).

Observations suggest that CO cores for clouds of similar virial mass are indeed smaller in the LMC than in the Milky Way, and most CO is photodissociated. The CO ( $J = 1 \rightarrow 0$ ) emission from LMC clouds is several times fainter than in the Milky Way (Cohen et al. 1988; Israel et al. 1993; Rubio, Lequeux, & Boulanger 1993; Kutner et al. 1997). Moreover, the  $I_{[\text{CII}]} / I_{\text{CO}}$  ratio in the LMC (which measures the fraction of carbon in PDRs) appears to be considerably enhanced with respect to the Milky Way (Mochizuki et al. 1994; Poglitsch et al. 1995; Israel et al. 1996).

## 2. Observations

In this study we discuss four new datasets on the N159/N160 region:  $^{13}\text{CO}$  ( $J = 1 \rightarrow 0$ ) at  $\nu \simeq 110.2020$  GHz,  $^{12}\text{CO}$  ( $J = 2 \rightarrow 1$ ) at  $\nu \simeq 230.5439$  GHz (Fig. 1),  $^{12}\text{CO}$  ( $J = 4 \rightarrow 3$ ) at  $\nu \simeq 461.0878$  GHz (Fig. 4), and [C I] ( $^{3}\text{P}_1 \rightarrow ^3\text{P}_0$ ) at  $\nu \simeq 492.1607$  GHz (Fig. 7). The first two were acquired using the Swedish-ESO Submillimeter Telescope (SEST) at La Silla, Chile, during May 1999. The latter two were made with the 1.7 m Antarctic Submillimeter Telescope and Remote Observatory (AST/RO, Stark et al. 1997b) at the Amundsen-Scott South Pole base, during the austral winter of 1998. Assuming an LMC distance of 52 kpc ( $D.M. \simeq 18.58$ ; Panagia, Gilmozzi, & Kirshner 1997), the “plate scale” for these observations is  $\approx 15$  pc per arcminute.

To complement these millimeter and submillimeter-wave datasets, we also use 21 cm H I and radio continuum data from the ATCA (Australia Telescope Compact Array) aperture synthesis survey of the LMC (Kim et al. 1998). Approximately three pointing centers were included in this map of the N159/N160 region. The zero-spacing flux, measured using the Parkes telescope, has been added to the ATCA data to obtain reliable column density estimates.

The  $^{13}\text{CO}$  ( $J = 1 \rightarrow 0$ ) transition is excited in almost all conditions found in molecular

clouds (gas kinetic temperature  $T_{kin} \gtrsim 5$  K and critical density  $n_{cr} \sim 1.7 \times 10^3$  cm $^{-3}$ ) and is generally used as a tracer of gas column density, since it is optically thinner than its isotopomer  $^{12}\text{CO}$ . The  $^{12}\text{CO}$  ( $J = 2 \rightarrow 1$ ) transition requires slightly warmer and denser gas to be excited ( $T_{kin} \gtrsim 11$  K,  $n_{cr} \sim 1.1 \times 10^4$  cm $^{-3}$ ), but these conditions prevail in all except the coldest and most diffuse molecular clouds. The excitation of the  $^{12}\text{CO}$  ( $J = 4 \rightarrow 3$ ) transition requires much warmer and denser gas ( $T_{kin} \gtrsim 55$  K,  $n_{cr} \sim 10^5$  cm $^{-3}$ ). Thus  $^{12}\text{CO}$  ( $J = 4 \rightarrow 3$ ) is excited only in the dense clumps and in the presence of heating sources. Finally, the [C I] ( $^3\text{P}_1 \rightarrow ^3\text{P}_0$ ) transition is excited in very general conditions ( $T_{kin} \gtrsim 23$  K,  $n_{cr} \sim 470$  cm $^{-3}$ ). Because C $^0$  is understood to be chiefly produced by the photodissociation of CO, this transition is thought to trace the warm PDR that forms in the surfaces of molecular clumps exposed to UV (we will, however, explore other alternatives later). The precise values of the critical density in all the above cases depend on the actual magnitude of radiative trapping effects, the ratio of ortho- and para-H $_2$ , and the kinetic temperature of the collisional partners, and are thus only approximate.

## 2.1. Millimeter Data

The bulk of the SEST data has system temperatures in the range 220–350 K at 230 GHz and  $T_{sys} \sim 190$ –250 K at 110 GHz. The maps were acquired during 1999 May, using the facility IRAM 115/230 GHz dual SIS receiver. The two frequencies were fed into the split high resolution acousto-optical spectrometer (AOS) backend. The resulting bandpasses ( $\sim 50$  km s $^{-1}$  for 230 GHz and  $\sim 100$  km s $^{-1}$  for 110 GHz) are more than adequate for the relatively narrow lines and small velocity variation inside N159/N160. The spectra were acquired in double beam switching mode, chopping 11.5' in azimuth. A few of the spectra showed contamination by emission in the off position, and these positions were reobserved at a different parallactic angle. At these frequencies the telescope has HPBW(230)  $\approx 23''$  and HPBW(110)  $\approx 48''$ , and the main beam efficiency is  $\eta_{mb}(230) \approx 0.50$  and  $\eta_{mb}(110) \approx 0.70$ .

The map was initially observed on a 24'' grid (i.e., approximately full-beam spacing at 230 GHz) and the brightest emitting regions were afterwards filled in on a 12'' grid (half-beam spacing). Two regions selected from the portion of the map showing low level emission were reobserved several times simultaneously in  $^{12}\text{CO}$  ( $J = 1 \rightarrow 0$ ) and ( $J = 2 \rightarrow 1$ ) (boxes in Fig. 1). Pointing and focus on a nearby SiO maser were performed before each observing session. The SEST pointing accuracy is 3'' rms.

## 2.2. Submillimeter Data

The  $^{12}\text{CO}$  ( $J = 4 \rightarrow 3$ ) AST/RO observations were made with a system temperature  $T_{sys} \sim 3500$  K. They were acquired on 15 May 1998 using the lower frequency side of AST/RO's 460/810 GHz dual SIS waveguide receiver. The [C I] ( ${}^3\text{P}_1 \rightarrow {}^3\text{P}_0$ ) observations had a system temperature  $T_{sys} \sim 1700$  K. The region was observed twice, on 1 July and 10 August of 1998, using the AST/RO SIS quasi-optical receiver. The backend in both cases was the 2048 channel low resolution AOS providing a spectral resolution  $\Delta v \sim 0.4 \text{ km s}^{-1}$  over a bandpass of  $\sim 350 \text{ km s}^{-1}$ . The spectra were acquired in position switching mode, chopping  $15'$  in azimuth (which is the same as R.A. at the pole).

The telescope was later determined to have HPBW(461)  $\sim 3.4' \pm 0.3$  and HPBW(492)  $\sim 3.8' \pm 0.3$ , using scans across the limb of the full Moon. The difference between the measured beams and the diffraction limited beam size for the telescope was caused by a  $2^\circ$  angular misalignment of the tertiary. No successful beam maps were acquired during the season, however, and the precise beam shape for either receiver is not actually known. Some of the source elongation manifested in the peaks of Fig. 4, for example, may not be intrinsic but caused by a distorted beam shape in that particular receiver.

The forward efficiency for AST/RO was determined from skydips to be 70%, and it is assumed to be identical to the main beam efficiency as the telescope is an off-axis, unblocked aperture dish. Thus we assume  $\eta_{mb} \approx 0.7$  for 461 and 492 GHz. The maps were observed on a  $30''$  grid, considerably oversampling the beam. A few of the spectra were contaminated by strong noise spikes that occasionally occur in two specific regions of the passband, possibly associated with electrical cross-talk between digital and analog signals in the AOS. These problematic spectra were discarded. Some grid points are therefore missing, but because of the oversampling this does not compromise the quality of the maps. The sensitivity of the [C I] map is  $1\sigma \approx 0.1 \text{ K km s}^{-1}$  in the central area, but somewhat worse at the edges because there the spatial averaging cannot take advantage of the heavy beam oversampling.

AST/RO's receivers sit on a static optical bench, located in the warm room below the dish, that does not track with the telescope. As a result any optical misalignment translates into precession of the receiver beam in the sky, a problem for faint sources that require long integrations. AST/RO's radio pointing was carefully controlled during the 1998 season by repeatedly observing a set of compact line emitting sources at different elevations and fitting a model that compensates for elevation-dependent pointing offsets and beam precession. Thus we are confident that the pointing accuracy during our observations was better than  $\sim 30''$  rms.

### 3. Discussion

#### 3.1. The Molecular ISM as Revealed by CO Observations

The CO dataset is composed of new  $^{13}\text{CO}$  ( $J = 1 \rightarrow 0$ ),  $^{12}\text{CO}$  ( $J = 2 \rightarrow 1$ ), and  $^{12}\text{CO}$  ( $J = 4 \rightarrow 3$ ) maps, as well as a preexisting  $^{12}\text{CO}$  ( $J = 1 \rightarrow 0$ ) map obtained by the SEST Magellanic Clouds key program. Figure 1 shows the  $^{12}\text{CO}$  ( $J = 2 \rightarrow 1$ ) and  $^{13}\text{CO}$  ( $J = 1 \rightarrow 0$ ) SEST data. The four main molecular peaks (Table 1) are apparent in both transitions: N160 to the north is a relatively weak and elongated cloud, N159W is the strongest peak in the complex, N159E appears to break up into three clumps at this resolution, and N159S is a triangular cloud with the smallest ( $J = 2 \rightarrow 1$ )/( $J = 1 \rightarrow 0$ ) intensity ratio in the complex. The cloud at offset  $\sim [+2', +5']$  is another member of the complex, which we will refer to as N160E. This cloud has very narrow lines (FWHM  $\sim 2.6$  km s $^{-1}$ ). In addition to the bridge connecting N159S with the northern portion of the complex, there is a wealth of extended, faint emission throughout the mapped region. It is important to stress this point: even below the 2 K km s $^{-1}$  contours essentially every position in this map shows a significant CO ( $J = 2 \rightarrow 1$ ) line if neighboring spectra are averaged. We will investigate the character of this extended, low level emission in §3.1.2.

The overall correspondence of these data with the published  $^{12}\text{CO}$  ( $J = 1 \rightarrow 0$ ) map (Johansson et al. 1994; Johansson et al. 1998) is extremely good, although some differences are apparent in the relative intensities and positions of the individual peaks. The shift in position is most noticeable for N159S, which at 1.3 mm appears to be  $\sim 21''$  eastward of its nominal 2.6 mm position. This offset is most probably not real, but caused by undersampling. These regions were mapped on a 30'' grid at ( $J = 1 \rightarrow 0$ ), while the SEST beam size at 115 GHz is 45'' (Johansson et al. 1998). Our own ( $J = 2 \rightarrow 1$ ) data are only sampled every 230 GHz beam (24'' grid) for N159S (N159E, N159W and N160 were observed on a 12'' grid). The CO ( $J = 2 \rightarrow 1$ ) peak in N159S falls almost precisely halfway between the ( $J = 1 \rightarrow 0$ ) samplings, and its position agrees very well with the fully sampled  $^{13}\text{CO}$  ( $J = 1 \rightarrow 0$ ) map. This suggests that the ( $J = 2 \rightarrow 1$ ) position for this core may be better than the ( $J = 1 \rightarrow 0$ ) location. Excitation gradients within N159S may also explain this positional discrepancy. Fortunately, the shifts in the position of the peaks are much smaller for the remaining clouds. To maintain consistency with previous work (e.g., Heikkilä et al. 1999) we use the CO ( $J = 1 \rightarrow 0$ ) positions tabulated in Table 1. Because the submillimeter data have much lower angular resolution the precise position of the peaks will not greatly affect the ratios in Table 3.

### 3.1.1. Physical Conditions

What are the physical conditions in the different clouds of the complex? Figure 2 compares the  $^{12}\text{CO}$  ( $J = 1 \rightarrow 0$ ), ( $J = 2 \rightarrow 1$ ), and the  $^{13}\text{CO}$  ( $J = 1 \rightarrow 0$ ) observations. All three datasets have been spatially smoothed to a common  $60''$  resolution, and the results for the regions of interest are summarized in Table 2. The  $^{13}\text{CO}/^{12}\text{CO}$  integrated intensity ratio is commonly used to estimate column density. The  $^{12}\text{CO}$  ( $J = 2 \rightarrow 1$ )/( $J = 1 \rightarrow 0$ ) line ratio is sensitive to density in the low density, optically thick limit, and to temperature for high densities (e.g., Kaufman et al. 1999). In the optically thin regime this ratio is sensitive to temperature, assuming that the emission is thermalized (for an exhaustive discussion of CO excitation see, however, Warin, Benayoun, & Viala 1996).

The centers of the N160 and N159W clouds have the highest  $^{13}\text{CO}/^{12}\text{CO}$  ( $J = 1 \rightarrow 0$ ) ratios and therefore the largest opacities, while at N159E this ratio is smaller by a factor of  $\sim 2$ . Conversely, N160 has the largest  $^{12}\text{CO}$  ( $J = 2 \rightarrow 1$ )/( $J = 1 \rightarrow 0$ ) ratio and therefore appears to be the hottest, while N159S is the coldest cloud in the complex. These conclusions agree broadly with a much more detailed multiline excitation analysis performed toward the main molecular peaks in the complex by Heikkilä et al. (1999), who find kinetic temperatures of 20, 25 and 10 K for N159W, N160 and N159S respectively.

The distribution of the warm and dense gas in the complex is elucidated by Fig. 4. Recall that the  $^{12}\text{CO}$  ( $J = 4 \rightarrow 3$ ) transition requires  $T \gtrsim 50$  K and  $n \sim 10^5 \text{ cm}^{-3}$  to be excited (§2). The angular resolution of the ( $J = 4 \rightarrow 3$ ) observations is  $\sim 4'$ , therefore all of the clouds are beam diluted and it is necessary to consider their beam-filling fractions to understand their relative intensities. All else being equal, larger clouds would appear brighter in Fig. 4. The peak of the CO ( $J = 4 \rightarrow 3$ ) map is N159W, due to a combination of intense emission and beam filling. Although there is an extension of ( $J = 4 \rightarrow 3$ ) emission in the southward direction, a peak at the position of N159S is most noticeably absent. Because N159W and N159S have similar sizes and intensities in the CO ( $J = 1 \rightarrow 0$ ) transition, this implies that the CO ( $J = 4 \rightarrow 3$ )/( $J = 1 \rightarrow 0$ ) ratio is much smaller for N159S.

Conversely, there is a hint of an emission peak at the position of N160, a small cloud in  $^{12}\text{CO}$  ( $J = 1 \rightarrow 0$ ). The presence of this peak suggests that the CO ( $J = 4 \rightarrow 3$ )/( $J = 1 \rightarrow 0$ ) ratio for N160 is large. These results for the ratios are confirmed by convolving the CO ( $J = 1 \rightarrow 0$ ) map to the resolution of the ( $J = 4 \rightarrow 3$ ) data (Table 3). The CO ( $J = 4 \rightarrow 3$ )/( $J = 1 \rightarrow 0$ ) ratio strongly depends on temperature and density, but the analysis performed by Heikkilä et al. (1999) shows that both clouds have volume densities above the ( $J = 4 \rightarrow 3$ ) transition critical density. Therefore the deficit of ( $J = 4 \rightarrow 3$ ) emission in N159S is mostly due to the much lower temperature of the southern

cloud. In the optically thick, LTE limit the observed CO ( $J = 4 \rightarrow 3$ )/( $J = 1 \rightarrow 0$ ) ratio corresponds to  $T_{kin} \sim 8$  K. This low temperature is probably due to the absence of star formation activity in N159S.

Figure 3 reveals the sources of heating and photodissociating radiation in the N159/N160 complex. The optical N159 nebula is centered between the N159E and N159W clouds. Portions of these clouds are in the foreground of the nebula and show themselves as obscurations against the bright background. The N160 cloud, however, appears to be behind its nebula. Part of the N160 nebulosity fills in the gap between the N160 and N160E molecular clouds, and is neatly delineated by them. N159S is seen here only as a subtle obscuration against the field stars, with no associated nebulosity. While all the other clouds have apparent embedded sources visible as peaks in the 60  $\mu$ m IRAS HIRES picture, N159S appears completely devoid of such sources. This lack of 60  $\mu$ m emission confirms the complete absence of any massive star-forming activity in the southern cloud.

### 3.1.2. *The Nature of the Extended CO Emission*

To investigate the faint extended emission apparent in the  $^{12}\text{CO}$  ( $J = 2 \rightarrow 1$ ) map, two small subregions at the edges of the complex (squares in Fig. 1) were mapped simultaneously in  $^{12}\text{CO}$  ( $J = 2 \rightarrow 1$ ) and ( $J = 1 \rightarrow 0$ ). This permitted us to obtain reliable line ratios for these two transitions. The average spectra for these two regions are shown in Fig. 5. The  $^{12}\text{CO}$  ( $J = 2 \rightarrow 1$ )/( $J = 1 \rightarrow 0$ ) ratio is  $\sim 3$  for both positions; about a factor of 2–4 larger than for the molecular peaks (cf., Table 2). For thermalized, optically thick CO, we expect a line ratio close to one. Larger ( $J = 2 \rightarrow 1$ )/( $J = 1 \rightarrow 0$ ) ratios can be produced by essentially only four mechanisms: 1) self or foreground-absorbed ( $J = 1 \rightarrow 0$ ) emission, 2) optically thick CO gas with temperature gradients, 3) different beam filling fraction for the ( $J = 1 \rightarrow 0$ ) and ( $J = 2 \rightarrow 1$ ) transitions, or 4) thermalized but optically thin CO emission.

In the first of these cases the lower transition is absorbed by either a cold cloud along the line of sight at similar velocities, or colder outer layers of the same cloud. If most of the CO in the absorbing gas is in the ground state (i.e., the intervening cloud is very cold) the ( $J = 2 \rightarrow 1$ ) transition will not suffer this effect, thereby artificially raising the ( $J = 2 \rightarrow 1$ )/( $J = 1 \rightarrow 0$ ) integrated intensity ratio. In case 2) the  $\tau = 1$  surface arises at different places along the line of sight for the two transitions. The observed line ratio will be the ratio of temperatures of the regions where the  $\tau = 1$  surface occurs. If there are temperature gradients in the cloud, then this ratio can in principle take any value. In case 3), because the opacity grows faster with  $N_{CO}$  in the ( $J = 2 \rightarrow 1$ ) than in the ( $J = 1 \rightarrow 0$ )

transition (Eq. A2), it is possible for the clumps to appear larger in the higher transition and consequently fill more of the beam. For this effect to be considerable it requires small and warm CO clumps (cf., Appendix A). In case 4) the ratio of both transitions will be in the range 0—4, depending on the temperature of the emitting CO gas (cf., Fig. 6). It can be shown that, in general, the ratio of integrated brightness temperatures for two consecutive rotational transitions in the optically thin, thermalized limit is

$$\frac{T_{(J+1) \rightarrow J}}{T_{J \rightarrow (J-1)}} = \left( \frac{J+1}{J} \right)^2 e^{-\frac{h\nu_{10}(J+1)}{kT_{ex}}} \quad (1)$$

where  $J$  is the rotational quantum number,  $T_{ex}$  is the excitation temperature, and  $h\nu_{10}/k \sim 5.5$  K for  $^{12}\text{CO}$ . For the transitions considered, a line ratio of  $\approx 3$  implies excitation temperatures  $T_{ex} \gtrsim 40$  K.

Which one of these possibilities is occurring in regions R1 and R2? The ( $J = 1 \rightarrow 0$ ) spectrum for R2 (Fig. 5) shows no clear evidence for self-absorption. Also, self-absorption tends to be a rather localized phenomenon: it is difficult to imagine it happening for two completely unrelated regions like R1 and R2. Thus we think it is an unlikely explanation. To decide among the remaining possibilities it would be ideal to be able to estimate the CO column density. The  $^{13}\text{CO}$  observations, however, are not sufficiently sensitive to provide useful limits for the  $^{12}\text{CO}/^{13}\text{CO}$  ratio and subsequently determine if the emission is optically thick.

Because some of the possibilities we are discussing require warm gas, it is important to consider the sources of heating in these two regions. Region R1 is located between the N160 and N159 nebulae, and consequently its temperature can easily be  $> 40$  K. Region R2 is found, however, in a quiescent region about  $4'$  ( $\sim 60$  pc projected distance) away from the center of the N159 nebula. To raise the gas temperature of region R2 to the  $\sim 40$  K needed to explain our ratios with optically thin CO emission, it is necessary to have heating sources. Surface temperature calculations of the PDR show that only a modest radiation field,  $\chi_{\text{uv}}$ , is required to produce that temperature ( $\chi_{\text{uv}} \sim 10$ , Kaufman et al. 1999). Eastward of N159S there are a few very faint and inconspicuous H II regions (DEM 272, 277 and 279, see Fig. 1; Davies et al. 1976), and traces of low level  $60\text{ }\mu\text{m}$  emission (Fig. 3). This suggests that photons, possibly from these H II regions or from their much brighter northern cousins, find their way there to heat the dust and elevate the temperature of the diffuse gas. Calculations in §3.2 show that the N159 nebula is probably bright enough to provide the  $\chi_{\text{uv}} \sim 10$  field needed to raise the temperature of the gas to 40 K. This radiation is not, however, intense enough to heat the core of N159S and make it a strong  $60\text{ }\mu\text{m}$  or CO ( $J = 4 \rightarrow 3$ ) emitter (Fig. 4). It is certainly not enough to produce any measurable 158

$\mu\text{m}$  [C II] emission, a transition that requires  $T \sim 92$  K to be excited (Fig. 7).

Given the fact that regions R1 and R2 are at the edges of the molecular cloud complex, we find the case for optically thin CO emission more compelling than the alternative explanations. It is, however, difficult to choose among possibilities 2), 3), and 4) with the available data. Nevertheless, we can make some specific predictions for the last two cases. In case 3) (larger beam-filling fraction for the  $(J = 2 \rightarrow 1)$  transition), simple geometric arguments show that very small CO clumps are required (Appendix A). These clumps are so small that they have only  $\tau \sim 2$  in the  $(J = 1 \rightarrow 0)$  transition and fill less than 1% of the beam. Future measurements of the  $(J = 3 \rightarrow 2)$  and  $(J = 4 \rightarrow 3)$  transitions in these regions may help distinguish between case 3) and optically thin emission (case 4). Because the ratio of opacities between the  $(J = 3 \rightarrow 2)$  and  $(J = 2 \rightarrow 1)$  transitions of CO is 2.25 for infinite temperature (Eq. 1), compared with 4 for  $\tau(J = 2 \rightarrow 1)/\tau(J = 1 \rightarrow 0)$ , the increase in beam filling fraction going from the  $(J = 2 \rightarrow 1)$  to the  $(J = 3 \rightarrow 2)$  transition will be only modest. Thus, assuming uniform density clumps in LTE we expect peak intensities  $T_{mb} \sim 0.18$  and 0.30 K in the  $^{12}\text{CO}$  ( $J = 3 \rightarrow 2$ ) transition for regions R1 and R2 respectively, only 20% brighter than the observed  $(J = 2 \rightarrow 1)$ . For clumps with density increasing toward the center the difference between the beam filling fraction for both transitions, and consequently the increase in brightness temperature, will be even smaller.

Concerning case 4), optically thin CO, the observed  $(J = 2 \rightarrow 1)$  intensities require CO column densities of  $N_{CO} \sim 2 \times 10^{15} \text{ cm}^{-2}$  assuming optically thin LTE emission at  $T_{ex} = 40$  K. A prediction of this model is that  $^{12}\text{CO}$  ( $J = 3 \rightarrow 2$ ) and  $(J = 4 \rightarrow 3)$  emission should be readily observable with peak intensities in a  $\sim 1'$  beam of  $T_{mb} \sim 0.25$  and 0.45 K for regions R1 and R2 respectively. Because of the low angular resolution of our  $^{12}\text{CO}$  ( $J = 4 \rightarrow 3$ ) data, however, we are not able to cleanly separate these regions from the nearby peaks that dominate the emission and therefore cannot test these models. Nevertheless, the fact that these regions are relatively bright in [C I] (§3.2.2), together with the results of column density calculations (§3.3), strongly suggest that they are part of a translucent, mostly photodissociated envelope.

### 3.2. Carbon in the Gas Phase of the ISM

Here we analyze the AST/RO [C I] ( ${}^3\text{P}_1 \rightarrow {}^3\text{P}_0$ ) map in conjunction with the available [C II] and CO data (Israel et al. 1997; Johansson et al. 1998). Figure 7 reveals the distribution of the three dominant forms of carbon in the gas phase of the ISM. The striking features of this map are the complex interplay between CO,  $\text{C}^0$  and  $\text{C}^+$ , and the fact that

[C I] peaks in the southern cloud, a quiescent region entirely devoid of strong UV sources.

Throughout the map there is an overall anticorrelation between the distributions of [C II] and [C I]. Only in N159W do the three species peak at approximately the same place, while in all the other clouds only two of the species show intense emission. The northern regions, with abundant star formation activity, are bright in [C II] but very dim in [C I]. The opposite is true for N159S. This cloud, with no massive star formation activity, is the peak of [C I] in the whole complex. It is also the region with the largest [C I]/CO intensity ratio (cf., Table 3). The [C I] emission in N159E is relatively faint, and the CO, C<sup>0</sup> and C<sup>+</sup> there appear to occupy adjacent and partially overlapping regions. Finally, in N160 a [C I] hole is filled in by a bright lobe of [C II], with a very faint ridge of [C I] emission overlapping with the CO.

The distribution of the different forms of gas phase carbon in N159/N160 may be affected by peculiarities of the region. For example, the central [C II] peak (N159-M, Israel et al. 1996), which has no FIR counterpart, is very close to the position of LMC-X1. It may be associated with that X-ray source, which is located at offsets  $\sim [-1', +1']$  (Fig. 1). LMC-X1, one of the strongest X-ray sources in the LMC, is a black-hole candidate with an O7 III companion star (Cowley et al. 1995; Schmidtke, Ponder, & Cowley 1999). It has been suggested that X-ray radiation has considerable effect on the chemistry of the ISM (e.g., Lepp & Dalgarno 1996), and it is possibly a way to produce C<sup>+</sup> and C<sup>0</sup>. Dissociation of CO in shocks may be another way of generating these species. Approximately 2' east of LMC-X1, Chu et al. (1997) have identified a supernova remnant, SNR 0540-697, based on optical spectra and X-ray data. This remnant is expanding at  $\sim \pm 150 \text{ km s}^{-1}$  and overlaps with most of the nebulosity NW of N159E (Fig. 3). We see no evidence in our data for [C I] emission at these velocities, and the ratio maps (Fig. 8) show no peculiar enhancement of the  $I_{[\text{CI}]}/I_{\text{CO}}$  and  $I_{[\text{CII}]}/I_{\text{CO}}$  ratios at the position of the remnant. Thus, shock-induced dissociation of CO does not appear to be an important mechanism producing [C II] or [C I] in this area.

On the spatial scale of these observations ( $1' \sim 15 \text{ pc}$ ) we do not expect to be resolving the PDRs into their three separate C<sup>+</sup>, C<sup>0</sup> and CO regions. This has been accomplished only in a few Galactic sources observable with much greater spatial resolution (e.g., the Orion bar). Accordingly, we expect to observe coextensive [C II], [C I] and CO emission for the molecular peaks. This is not necessarily the case for the translucent medium. In diffuse gas and in the presence of strong UV sources most carbon will be ionized. Thus C<sup>+</sup> will dominate the emission, forming [C II] regions akin to Strömgren spheres around the ionizing sources. This is apparently happening in the northern portion of the map where bright lobes of [C II] emission east and west of N160 fill in holes in the [C I] distribution. These

[C II] peaks and [C I] holes are unequivocally associated with H II regions (Fig. 9). Most of their [C II] emission may arise from C<sup>+</sup> mixed with H II inside the Strömgren sphere, collisionally excited by electrons.

In principle, over a small range of extinction ( $A_V \sim 0.3 - 1$ ) we could have clouds where C<sup>+</sup> and C<sup>0</sup> are dominant, with little or no CO emission. That may be occurring between N160 and N159W, where bright [C II] and [C I] overlap in a region that shows little CO emission. One must be careful, however, when interpreting and combining data with very different (and, for the [C I], low) angular resolutions. Figure 7b shows the three transitions convolved to a common resolution ( $\sim 4.3'$ ). In this map there are only two peaks in the [C II] distribution (N160 and N159W), and the [C II], [C I] and CO maxima near N159W are displaced by about 1' from each other in a way that resembles a PDR C<sup>+</sup>/C<sup>0</sup>/CO transition. This structure, however, is not a PDR: if these clouds were moved to Orion (0.5 kpc away and perhaps the best example of a resolved PDR) the distance between the [C II] and the CO peaks would span 2 degrees in the sky. What we are observing are large scale excitation and chemical gradients. The extended [C II] emission is heavily weighted in the convolved data and pulls the overall maximum northward, also diluting the peak coincident with N159W. In much the same manner, the ( $J = 1 \rightarrow 0$ ) peak is pulled southward by the extended CO emission. Notice that the CO maximum near N159S moves westward for the same reason.

### 3.2.1. The Neutral Carbon Emission from N159S

The fact that the peak of [C I] emission for the entire complex is a quiescent region is unexpected if C<sup>0</sup> has, chiefly, a PDR origin and thus requires UV photons to be produced. To review the evidence: N159S is a dark cloud with weak CO ( $J = 4 \rightarrow 3$ ) emission (hence at a low temperature), with no conspicuous heating sources apparent in the optical or the FIR (hence little or no star formation), and with very faint [C II] emission (hence no UV sources). Nevertheless, according to the analysis by Heikkilä et al. (1999) it is the cloud with the largest column density in the complex ( $N_{H_2} \sim 1.7 \times 10^{22} \text{ cm}^{-2}$ ,  $A_V \sim 4.5$  compared to  $N_{H_2} \sim 1.1 \times 10^{22} \text{ cm}^{-2}$ ,  $A_V \sim 2.9$  for N159W and N160), and it is also the brightest [C I] emitter, possessing the largest  $I_{[CI]}/I_{CO}$  ratio. This is certainly indirect evidence, but it suggests that most of the C<sup>0</sup> in this cloud originates not by UV photodissociation of CO in the PDR, but inside the CO cores.

Recent modeling results indicate, however, that the  $I_{[CI]}/I_{CO}$  ratio is very insensitive to the radiation field (Kaufman et al. 1999). Therefore only a small amount of UV radiation is necessary to explain the observed ratio in the context of a PDR. This can

be understood in the following way: in  $A_V$  space the extent of the [C I] emitting region in a homogeneous one-dimensional calculation, and consequently the  $C^0$  column density, is relatively insensitive to the input radiation field. The depth at which the  $C^+/C^0/CO$  transition occurs, however, increases for larger  $\chi_{uv}$ . Because  $^{12}CO$  becomes optically thick soon after this transition, neither the [C I] nor the CO emerging intensities are a strong function of the radiation field at the surface of the cloud. All the molecular peaks in this region feature optically thick  $^{12}CO$ , based on the  $^{13}CO/^{12}CO$  intensity ratios listed in Table 2 ( $^{12}C/^{13}C \sim 50$  for the LMC, Johansson et al. 1994).

The previous reasoning applies to homogeneous clouds with plane-parallel (i.e., one-dimensional) geometry. If molecular clouds are in fact clumpy, they can be modeled as an ensemble of spherical clouplets. In this scenario the UV field should have a dramatic effect on the  $C^+$ ,  $C^0$  and CO column densities and intensity ratios. In a clump subjected to an increasing UV field, the CO emitting region can be pushed towards the center only as far as the radius of the clump, after which the entire clump photodissociates. This scenario has been modeled in detail by Bolatto et al. (1999). Following those calculations we expect an inverse dependence between  $\chi_{uv}$  and CO column density, and a modest increase in the [C I]/CO ratio for increasing  $\chi_{uv}$  (growing by  $\approx 25\%$  per order of magnitude in  $\chi_{uv}$ ). This model, however, does not include an interclump medium. Modeling of clumpy PDRs as a collection of high-extinction ( $A_V \sim 100$ ), dense regions immersed in a diffuse interclump gas exposed to high  $\chi_{uv}$  (Meixner & Tielens 1993, 1995) suggests that most of the CO ( $J = 1 \rightarrow 0$ ) and [C I] emission comes from the low density interclump medium. Thus, at low UV fields and low clump filling fractions, and when considering interclump dominated lines, a clumpy PDR may behave very similarly to a homogeneous plane-parallel model of interclump density. Similarly, at high clump filling fractions the contribution from the interclump medium would be unimportant.

We will now try to estimate the radiation field in the N159S region. This cloud is most likely illuminated by the bright northern H II regions, although there may be a small contribution from the much smaller nearby regions mentioned in §3.1.2 (Figs. 1, 3). Estimates for the luminosities and possible exciting sources of the FIR peaks in the N159/N160 complex, based on IRAS HIRES data, are given in Table 4. These estimates are in reasonably good agreement with the KAO results by Israel et al. (1996). An equivalent spectral type and multiplicity is assigned to each flux, by assuming that all of the starlight is trapped by the dust and reradiated in the FIR.

In order to use these results to estimate the UV radiation field far away from these sources we will assume that the radiation intercepted by dust is only a fraction  $f$  of the total luminosity, and therefore a fraction  $(1 - f)$  escapes the star-forming region and the

enshrouding dust. Furthermore, we will assume that about 50% of the luminosity of the exciting stars is emitted in the range 912–2066Å (typical for late O/early B-type stars). Therefore the UV radiation field at a distance  $d$  is

$$\chi_{\text{uv}} \approx \frac{(1-f)L_{\text{FIR}}}{8\pi f \chi_0 d^2} \quad (2)$$

where  $\chi_0$  is the standard normalization factor (approximately the UV radiation field in the vicinity of the Sun,  $\chi_0 = 1.6 \times 10^{-3}$  erg s<sup>-1</sup> cm<sup>-2</sup>; Habing 1968). Using this formula we can compute  $\chi_{\text{uv}}$  for N159S, assuming that it is illuminated by the nearby N159 H II region. At the projected distance  $d \sim 90$  pc, and assuming that 90% of the UV escapes the surrounding dust, we obtain  $\chi_{\text{uv}} \simeq 60$ . If only 50% of the UV escapes then the radiation field would be  $\chi_{\text{uv}} \simeq 6$ . By comparison, radiation field estimates by Israel et al. (1996) for the northern clouds N159E-W and N160 near H II regions range from 300–600 (cf., Table 1). Our  $\chi_{\text{uv}}$  estimate for N159S is probably too large, since: 1) we use the projected distance, and 2) we assume no dust extinction between the northern H II regions and N159S.

Another way of computing the luminosity of the UV sources in this region is to use the radio continuum information. The 21 cm radio continuum data (Figure 9) poses constraints similar to the FIR on the luminosity of the stars that excite the H II regions. In Table 5 we have calculated the spectral type and multiplicity, assuming optically thin free-free emission and following Jackson & Kraemer (1999) analysis. These estimates are generally lower than those based on the FIR, mostly because spectral types later than O6 are still very luminous (adding to the FIR luminosity) but contribute little to the radio continuum. Recent ISOCAM observations (Comerón & Claes 1998), for example, reveal three strong 15  $\mu\text{m}$  peaks in N159 which feature very faint radio continuum, and are thus attributed to ultra-compact H II regions which are optically thick at 21 cm. These are examples of sources that would add to the FIR luminosity but be invisible at 1.42 GHz. Nevertheless, both the radio continuum and the FIR measurements agree within a factor of  $\sim 2$  ( $L_{\text{FIR}} \sim 2 L_{\text{RC}}$ ), strongly suggesting that most UV is actually intercepted by the surrounding dust. Taking into account the various estimates and caveats discussed in the previous paragraph, we conclude that  $\chi_{\text{uv}}(\text{N159S}) \lesssim 10$ . Such a low UV field is consistent with the faint [C II] emission from N159S, as well as its low  $I_{\text{[CII]}}/I_{\text{CO}}$  ratio.

Even orders of magnitude in  $\chi_{\text{uv}}$ , however, have little impact on the value of the  $I_{\text{[CII]}}/I_{\text{CO}}$  ratio in standard PDR plane-parallel models. According to the calculations by Kaufman et al. (1999), the [C I]/CO intensity ratio observed in N159S can be attributed to gas with  $n \approx 10^5$  cm<sup>-3</sup> at  $\chi_{\text{uv}} \sim 1-10^5$ . Note that metallicity has only very small effects on plane-parallel model calculations, for reasons essentially similar to those discussed for  $\chi_{\text{uv}}$ .

Thus, although the aforementioned calculations were performed for Galactic sources their results can be safely applied to the LMC. The coincidence between this density and that obtained by Heikkilä et al. (1999) for N159S appears satisfying, until we take into account the different scale of the measurements: the  $4'$  (60 pc) region over which  $I_{[CI]}/I_{CO} \simeq 0.15$  is  $\approx 25$  times larger than the SEST  $\sim 48''$  beam used to carry out the multiline excitation analysis. This is an extremely high density for such a large region. Invoking beam filling fraction arguments avoids this problem, by assuming that only small and dense regions within the beam are dominating the CO ( $J = 1 \rightarrow 0$ ) and [C I] emission. Comparison of the measured [C I] intensity with the model results suggests  $\sim 10\%$  beam filling fraction. Nevertheless, if such a high density is characteristic of the gas producing the [C I] emission, it rules out the interclump medium as the main reservoir of neutral carbon. Meixner & Tielens' (1995) modeling of two-phase (clump + interclump) PDRs shows that  $I_{[CI]}/I_{CO} \sim 10$  can be obtained for a mixture of  $5 \times 10^5 \text{ cm}^{-3}$   $A_V \sim 100$  clumps immersed in a  $3 \times 10^3 \text{ cm}^{-3}$  diffuse component, with 20% volume filling fraction for the clumps. These computations, however, were carried out for  $\chi_{uv} \sim 5 \times 10^4$  and no similar calculations are available for UV fields closer to that of N159S.

At the beginning of this section we pointed out a series of intriguing facts about N159S that may suggest a non-PDR origin for most of its neutral carbon. Despite them, however, we conclude that the observed [C II], [C I], and CO intensities in N159S are consistent with standard PDR theory assuming  $n \approx 10^5 \text{ cm}^{-3}$  and  $\chi_{uv} \sim 10$ . These values of the density and UV field agree with previous excitation analysis and with the best estimates of  $\chi_{uv}$  in N159S, assuming it is illuminated by the northern complex of H II regions.

### 3.2.2. The $I_{[CI]}/I_{CO}$ Ratio in the Complex

How are the relative intensities of the different forms of carbon affected by the local conditions? In the previous sections we have seen that [C I] is dim in the northern portion of the map, where there is active massive star formation, and bright in N159S. In this section we will compare the  $I_{[CI]}/I_{CO}$  and  $I_{[CII]}/I_{CO}$  ratios throughout this region, and look for the effects of radiation fields and metallicity.

Figure 8 shows the  $I_{[CI]}/I_{CO}$  and  $I_{[CII]}/I_{CO}$  ratios mapped for the entire complex, with the data convolved to a common  $4.3'$  resolution. Table 3 shows our  $I_{[CI]}/I_{CO}$  results tabulated for the regions of interest. Notice that Table 3 uses a  $4'$  beam size. To convert from intensity ratios given in  $\text{K km s}^{-1}$  to ratios in  $\text{erg s}^{-1} \text{ cm}^{-2} \text{ sr}^{-1}$  multiply by  $\sim 78$  for  $I_{[CI]}/I_{CO}$ . Since N160 is such a weak [C I] source, its ratio is dominated by the surrounding extended [C I] emission and therefore the ratio increases noticeably when measured in a

larger beam. For N159S the angular resolution of the measurement is unimportant, and the ratio remains mostly unchanged. Therefore the high  $I_{[CI]}/I_{CO}$  ratio at N159S is not an artifact caused by the nearby emission. The first measurement of the [C I]/CO intensity ratio in N159 was carried out by Stark et al. (1997a), who obtained  $I_{[CI]}/I_{CO} \simeq 0.26$  (intensities in  $K \text{ km s}^{-1}$ ). This determination was based on a single spectrum taken towards the nominal position of N159W, and assumed an unresolved structure for the CO from this cloud. We find that, albeit in a larger beam,  $I_{[CI]}/I_{CO} \simeq 0.12$  for N159W. This difference is largely due to an underestimate of the CO intensity in the aforementioned paper.

Two regions of the map feature high [C I]/CO intensity ratios: the northern region, where there  $I_{[CII]}/I_{CO}$  also peaks, and the southeast corner, where there is extended low-level CO ( $J = 2 \rightarrow 1$ ) but little ( $J = 1 \rightarrow 0$ ) emission and no detectable [C II] emission. We think that in both cases we are seeing translucent, mostly photodissociated gas, with the important difference that the abundant UV radiation in the northern region raises the temperature of the PDRs over the 91.3 K required to excite the 158  $\mu\text{m}$  [C II] transition (see §3.3). There is the possibility that the southeastern extension of the N159S cloud in [C I] is an artifact of the sampling, since the map is missing a few spectra there. Because of the heavy oversampling of the beam, however, we think that this extension is probably real. It appears also that there is a modest increase in the  $I_{[CI]}/I_{CO}$  ratio at the edges of the complex, and perhaps in the immediate vicinity of LMC-X1. The lowest ratios are found south of N159W.

How does the  $I_{[CI]}/I_{CO}$  ratio in this complex compare with the  $I_{[CII]}/I_{CO}$  ratio? Since both  $\text{C}^+$  and  $\text{C}^0$  are produced by the action of UV photons in the PDR, the naive expectation is that [C II] and [C I] should have a similar distribution in unresolved PDRs. Excitation differences, important for very low radiation fields ( $\chi_{\text{uv}} < 10$ ), will become negligible for  $\chi_{\text{uv}} > 100$  as the PDR reaches temperatures well over 100 K (Kaufman et al. 1999). As discussed at the beginning of §3.2 there are other reasons why we may not expect [C II] and [C I] to be coextensive in the diffuse translucent gas, namely the formation of  $\text{C}^+$  “Strömgren spheres” near UV sources. In these regions carbon ionization and not dust absorption is the dominant process that removes UV photons, and consequently all the carbon is in the form of  $\text{C}^+$ . In the molecular material, however, UV photons should be predominantly removed by dust grains, leaving a fraction of the carbon in the form of  $\text{C}^0$ . Consequently, if the structure of the ISM is clumpy and therefore allows the UV photons to penetrate deep into the clouds, the expectation is for [C I] and [C II] to be coextensive and in many ways behave similarly. In particular, modeling of clumpy PDRs suggest that both the  $I_{[CII]}/I_{CO}$  and  $I_{[CI]}/I_{CO}$  ratio should be enhanced in low metallicity systems (Bolatto et al. 1999). This is mostly due to the rapidly dwindling sizes of the CO cores of the clumps with decreasing metallicity and dust-to-gas ratio.

The [C II]/CO intensity ratio has been studied in a variety of systems (e.g., Stacey et al. 1991), and the highest ratios are associated with low metallicity environments. As we pointed out in §1, Mochizuki et al. (1994) found a considerable enhancement of the global  $I_{\text{[CII]}}/I_{\text{CO}}$  ratio of the LMC ( $I_{\text{[CII]}}/I_{\text{CO}} \approx 23,000$ ) over that of the Milky Way. Average ratios for Galactic objects are  $I_{\text{[CII]}}/I_{\text{CO}} \sim 1,300$  for GMCs, and  $\sim 4,400$  for H II regions (Stacey et al. 1991). Observations by Israel et al. (1996) of N159/N160 (cf., Table 1) show that the three northern molecular peaks (N159E, N159W and N160) have  $I_{\text{[CII]}}/I_{\text{CO}}$  ratios 1–5 times larger than comparable Galactic regions while their  $I_{\text{FIR}}/I_{\text{CO}}$  ratios are 3–40 times lower, suggesting a much larger abundance of  $\text{C}^+$ . Measurements of the 30 Doradus region (Poglitsch et al. 1995) yielded a ratio  $I_{\text{[CII]}}/I_{\text{CO}} \approx 65,000$  for its molecular peaks. Madden et al. (1997) studied the global [C II] emission from the low metallicity dwarf galaxy IC 10 which has  $Z_{\text{IC10}} \approx Z_{\text{MW}}/4$  (where we have used the oxygen abundance in Orion as representative of the Galaxy,  $12 + \log[\text{O}/\text{H}] \approx 8.75$ ; Lequeux et al. 1979). They found ratios in the range  $I_{\text{[CII]}}/I_{\text{CO}} \sim 14,000$ – $87,000$  for various regions.

Unlike the widely varying  $I_{\text{[CII]}}/I_{\text{CO}}$  ratio, the  $I_{\text{[CI]}}/I_{\text{CO}}$  ratio for the molecular peaks of N159/N160 is surprisingly uniform. The values range only between  $I_{\text{[CI]}}/I_{\text{CO}} \sim 7$  to  $\sim 12$ . These are very similar to the typical ratio in the Milky Way where  $I_{\text{[CI]}}/I_{\text{CO}} \sim 13$  (intensities in  $\text{erg s}^{-1} \text{cm}^{-2} \text{sr}^{-1}$ ). This is not an isolated result. Wilson (1997) observed the [C I] emission from several clouds at different galactocentric distances in M 33, a spiral galaxy with a well-known metallicity gradient. She obtained ratios of  $I_{\text{[CI]}}/I_{\text{CO}} \sim 3$ – $14$  and found no obvious trend with inferred metallicity. Recently, Bolatto et al. (2000) studied the  $I_{\text{[CI]}}/I_{\text{CO}}$  ratio in the molecular cloud complex associated with the brightest star-forming region of IC 10. They obtained an average ratio  $I_{\text{[CI]}}/I_{\text{CO}} \sim 18$ , only slightly larger than the average Galactic ratio. Finally, Gerin & Phillips' (2000) recent study of atomic carbon in a variety of galaxies finds some dispersion in the  $I_{\text{[CI]}}/I_{\text{CO}}$  intensity ratio, but no clear segregation with galaxy type. Their sample of galaxies has an average ratio  $I_{\text{[CI]}}/I_{\text{CO}} \sim 16$ , with most ratios found in the interval  $I_{\text{[CI]}}/I_{\text{CO}} \sim 8$ – $32$ .

Overall, if there is a trend for  $I_{\text{[CI]}}/I_{\text{CO}}$  with metallicity it is certainly much weaker than the one observed for  $I_{\text{[CII]}}/I_{\text{CO}}$ . A plausible explanation for the constancy of the [C I]/CO intensity ratio is a non-PDR origin for a fraction of the  $\text{C}^0$ . While it seems unequivocal that in the diffuse gas most neutral carbon is associated with PDRs, it is possible that a different mechanism dominates its production inside molecular cloud cores. If  $\text{C}^0$  is indeed produced in these cores by processes unrelated to photochemistry, it would simply explain the close observed association between the [C I] and CO line intensities.

### 3.3. The Column Density in the Extended Envelope

The entire molecular cloud complex appears to be surrounded by an extended envelope visible in CO ( $J = 2 \rightarrow 1$ ), and possibly [C I] and [C II]. For example, the extended and relatively bright [C I] emission east of N159S and south of N159E correlates very well with the faint, extended CO ( $J = 2 \rightarrow 1$ ) in the same region, as does the tongue of [C I] spreading north of the N159 nebula. Assuming, as was discussed in §3.1.2, that the CO emission in this region is optically thin, then we appear to be seeing translucent gas emitting in [C I]. Translucent clouds are clouds with visual extinction  $A_V \lesssim 1$ , where an important fraction of the carbon is in the form of  $C^+$  and  $C^0$  (e.g., Ingalls et al. 1997). While the regions surrounding R1 are strong [C II] emitters, region R2 and its environs are very faint in [C II]. Undetected by Israel et al. (1996), the upper limit for the integrated intensity from R2 is  $I_{[CII]} \sim 6.8 \times 10^{-5} \text{ erg s}^{-1} \text{ cm}^{-2} \text{ sr}^{-1}$ . The limit for the corresponding  $C^+$  column density, derived for the high-temperature, high-density case (that is, the minimum column density corresponding to the intensity limit) is  $N_{C^+} \lesssim 4 \times 10^{16} \text{ cm}^{-2}$ , about 20 times larger than the corresponding column density of CO derived in §3.1.2. Singly ionized carbon could well be the dominant form of carbon in this region yet remain undetected.

Assuming that most of the carbon is in the form of  $C^+$ , we can estimate the hydrogen column density along these lines of sight. For R1,  $I_{[CII]} \approx 1.4 \times 10^{-4} \text{ erg s}^{-1} \text{ cm}^{-2} \text{ sr}^{-1}$ , therefore  $N_{C^+} \sim 8 \times 10^{16} \text{ cm}^{-2}$ . Assuming an LMC gas phase carbon abundance per H nucleus  $x_C \sim 7 \times 10^{-5}$  (Dufour 1984), this yields  $N_H \sim 1.2 \times 10^{21} \text{ cm}^{-2}$ , or  $A_V \sim 0.15$  (using the conversion factor  $1 A_V \sim 8 \times 10^{21} \text{ cm}^{-2}$  which is four times that of the Galaxy). In the case of R2, where no [C II] is detected, Fig. 7b shows that there is some very low level emission that becomes statistically significant only after spatial smoothing. We will assume  $I_{[CII]} \sim 3 \times 10^{-5} \text{ erg s}^{-1} \text{ cm}^{-2} \text{ sr}^{-1}$  (about half the sensitivity limit). In the high-temperature, high-density limit this would result in  $N_H \sim 4 \times 10^{20} \text{ cm}^{-2}$ , or  $A_V \sim 0.05$ . If we allow for a relatively low PDR temperature,  $T_{kin} \sim 40 \text{ K}$ , consistent with a low  $\chi_{uv}$  and the optically thin CO analysis, we find  $A_V \sim 0.15$ . It is important to point out that these are line-of-sight extinctions, and not necessarily equal to the  $A_V$  that extinguishes the UV field and enters the PDR calculation. For a completely edge-on PDR, for example, these two extinctions would be measured along orthogonal directions and thus be unrelated. If this gas fills the beam and has a density near the critical density of [C II] ( $n_{cr} \sim 3 \times 10^3 \text{ cm}^{-3}$ ), as we implicitly assumed in the calculations, then we are seeing a  $\sim 0.1 \text{ pc}$  thick layer of gas. We find this sheet-like geometry, with a sheet thickness of only 1/100 of the extent in the plane of the sky, uncomfortable although not impossible.

How do these results compare with column density predictions based on the H I data? We assume a spin temperature of  $T_{sp} \sim 110\text{--}180 \text{ K}$  based on the H I absorption observed

towards the N159 continuum sources (Spitzer 1978). We can then compute atomic hydrogen column densities of  $N_H \sim 4.2 \times 10^{21} \text{ cm}^{-2}$  and  $N_H \sim 4.5 \times 10^{21} \text{ cm}^{-2}$  for regions R1 and R2 respectively. These column densities are  $\sim 3$  times larger than those derived from  $I_{[\text{CII}]}$ . The gas is apparently hot enough to populate the upper fine structure level of  $\text{C}^+$  and excite the  $158 \mu\text{m}$  [C II] transition (recall  $h\nu/k = 91.3 \text{ K}$  for [C II]), thus this discrepancy is probably not due to temperature effects.

This method, however, is not very precise since it heavily relies on similar excitation conditions for the H I seen in absorption and emission, and this assumption is compromised by the large scales involved in the map (recall  $1' \sim 15 \text{ pc}$ ). Other possible causes for the apparent discrepancy in  $N_H$  are: 1) a deficiency of  $\text{C}^+$  in the atomic gas (only 30% of the C is photoionized), 2) the volume density of the atomic gas is low, and consequently the excitation of [C II] is subthermal ( $n < n_{cr}([\text{C II}])$ ), or 3) there are density fluctuations within the beam, and the [C II] emission is dominated by the fraction of the  $\text{C}^+$  column that is thermalized ( $n > n_{cr}([\text{C II}])$ ).

The first possibility appears to be very improbable, since unless the material is well shielded from the UV most of the carbon should be in the form of  $\text{C}^+$  rather than  $\text{C}^0$ . Unfortunately the large beam in our [C I] observations makes impossible to separate cleanly these regions from the molecular peaks, thus precluding us from obtaining a reliable estimate for the column density of  $\text{C}^0$  in R1 and R2. Subthermal excitation of  $\text{C}^+$  requires the density of H I to be below the critical density of the  $158 \mu\text{m}$  transition,  $n_{cr} \approx 3000 \text{ cm}^{-3}$ . The intensity  $I_{[\text{CII}]}$  of  $\text{C}^+$  collisionally excited by H atoms can be computed using (e.g., Madden et al. 1997):

$$I_{[\text{CII}]} = 2.35 \times 10^{-21} N_{\text{C}^+} \left[ \frac{2 \exp(-h\nu/kT)}{1 + 2 \exp(-h\nu/kT) + n_{cr}/n} \right] \quad (3)$$

where  $h\nu/k = 91.3 \text{ K}$ . Consequently, a discrepancy of a factor of 3 would require  $n \sim 500 \text{ cm}^{-3}$ , well below the critical density of [C II]. Notice that this density would bring the physical thickness of the [C II] emitting layer to  $\sim 3 \text{ pc}$ . The third possibility (density fluctuations within the beam, akin to clumping) would make the regions where  $n > n_{cr}$  dominate the [C II] emission (about 1/3 of the total column), while in most of the gas  $n \ll n_{cr}$  and the [C II] excitation is subthermal. This ought to be happening at some level, because CO ( $J = 2 \rightarrow 1$ ) is present throughout the region and its excitation requires  $n \sim 10^4 \text{ cm}^{-3}$ . This density is probably too large to be the average volume density in the envelope, thus most of the CO and perhaps a large fraction of the [C II] emission is originating in clumps within the envelope.

#### 4. Summary and Conclusions

We have discussed new  $^{13}\text{CO}$  ( $J = 1 \rightarrow 0$ ),  $^{12}\text{CO}$  ( $J = 2 \rightarrow 1$ ),  $^{12}\text{CO}$  ( $J = 4 \rightarrow 3$ ), and  $[\text{C I}]$  ( ${}^3\text{P}_1 \rightarrow {}^3\text{P}_0$ ) emission line maps of the N159/N160 molecular cloud complex of the Large Magellanic Cloud.

The  $^{12}\text{CO}(J = 2 \rightarrow 1)$  map shows extended faint emission previously undetected in the ( $J = 1 \rightarrow 0$ ) transition. Further analysis of the ( $J = 2 \rightarrow 1$ )/( $J = 1 \rightarrow 0$ ) intensity ratio in two selected subregions (R1 and R2) shows that this ratio is  $\gtrsim 3$  for the extended low level emission. This high value indicates optically thin CO emission from warm gas ( $T_{\text{kin}} \geq 40$  K). The  $I_{[\text{CI}]}/I_{\text{CO}}$  ratio for R1 and R2 appears modestly enhanced with respect to the molecular peaks (Fig. 8). The  $I_{[\text{CII}]}/I_{\text{CO}}$  ratio is large for the northern region (R1), but  $[\text{C II}]$  was not detected by Israel et al. (1996) towards region R2. Because of the low UV field heating the ISM in the southern region, this may be a temperature effect. The gas in the southern portion of the complex, far away from the massive star formation and bright H II regions, is too cold to excite the  $158 \mu\text{m}$  transition ( $T < 92$  K). The faint CO envelope appears to be translucent ( $A_V < 1$ ), and column density calculations assuming that  $\text{C}^+$  is the dominant form of carbon confirm this result. The column density derived from the neutral hydrogen 21 cm data appears to be  $\sim 3$  times larger than  $N_H$  obtained from  $[\text{C II}]$ . This is probably caused by density enhancements (clumping) within the beam.

The  $^{12}\text{CO}(J = 4 \rightarrow 3)$  map shows that the ( $J = 4 \rightarrow 3$ )/( $J = 1 \rightarrow 0$ ) intensity ratio is  $\sim 4$  times larger in the northernmost cloud (N160) than in the southern cloud (N159S). This agrees very well with indicators of star formation activity ( $I_{\text{FIR}}$ ,  $I_{[\text{CII}]}$ , radio continuum), and is probably due to the much lower temperature of the quiescent southern cloud. Estimates of the radiation field incident on N159S suggest  $\chi_{\text{uv}} \lesssim 10$ , consistent with a low temperature. The ratio of 100/60  $\mu\text{m}$  continuum also indicates a low temperature.

The  $[\text{C I}]$  ( ${}^3\text{P}_1 \rightarrow {}^3\text{P}_0$ ) map shows the  $[\text{C I}]$  intensity and the  $I_{[\text{CI}]}/I_{\text{CO}}$  ratio for the molecular concentrations peaking in N159S. The observed values are consistent with the PDR computations available for homogeneous, plane-parallel models, at  $n \sim 10^5 \text{ cm}^{-3}$  and  $\chi_{\text{uv}} \sim 10$ . Because in those models  $I_{[\text{CI}]}$  is not sensitive to  $\chi_{\text{uv}}$ , however, the presence of intense  $[\text{C I}]$  emission in N159S is not a good test for a possible non-PDR origin for  $\text{C}^0$  inside GMCs. There is pervasive  $[\text{C I}]$  emission throughout the region between N159EW and N160. This region also emits strongly in  $[\text{C II}]$ , and features some of the largest  $I_{[\text{CI}]}/I_{\text{CO}}$  and  $I_{[\text{CII}]}/I_{\text{CO}}$  ratios in the complex. The radio continuum sources embedded in this gas appear as holes in the  $[\text{C I}]$  distribution, while they are peaks in the  $[\text{C II}]$ . The  $[\text{C II}]$  in these peaks probably originates inside the H II regions, mostly excited by collisions with electrons.

The [C I]/CO intensity ratios measured in the molecular peaks of the complex range between  $I_{[CI]}/I_{CO} \sim 7\text{--}12$  (intensities in  $\text{erg s}^{-1} \text{cm}^{-2} \text{sr}^{-1}$ ). This ratio is similar to the average ratio in the Milky Way ( $I_{[CI]}/I_{CO} \approx 13$ ) and to that measured in the low metallicity dwarf IC 10 ( $I_{[CI]}/I_{CO} \sim 18$ , Bolatto et al. 2000). The [C I]/CO intensity ratio for the translucent gas is somewhat larger,  $I_{[CI]}/I_{CO} \sim 20\text{--}30$ . While intense [C II] ( ${}^2\text{P}_{3/2} \rightarrow {}^2\text{P}_{1/2}$ ) emission and large  $I_{[CII]}/I_{CO}$  ratios appear to be unequivocally associated with massive star formation, [C I] ( ${}^3\text{P}_1 \rightarrow {}^3\text{P}_0$ ) emission and the  $I_{[CI]}/I_{CO}$  ratio shows no such clear association and has a much more complex behavior. The  $I_{[CI]}/I_{CO}$  ratio is more uniform than the  $I_{[CII]}/I_{CO}$  ratio throughout the complex, where spans values of  $I_{[CI]}/I_{CO} \sim 5\text{--}25$  whereas  $I_{[CII]}/I_{CO}$  ranges between  $\sim 500\text{--}25,000$  (i.e., a factor of 5 versus a factor of 50). This is partially due to the more stringent excitation conditions required by [C II].

We believe that our understanding of the ISM, especially the actively star-forming ISM, can be enormously advanced by further studies of the Magellanic Clouds. These galaxies, with their proximity, their active star formation, their low metallicities, and their unobscured lines of sight, present unique opportunities for detailed multiwavelength studies. Among the different regions in the Clouds, the N159/N160 complex is located at a privileged place, between the violent starburst of 30 Doradus and the quiescent southern CO ridge. Because of its location, its distinct environments, and the wealth of phenomena taking place within its bounds, the N159/N160 complex is one of the most interesting places in the Magellanic Clouds. Unfortunately, these galaxies are out of the reach of the large radioastronomy facilities in the Northern Hemisphere. The advent of some of the observatories now being planned, such as the Atacama Large Millimeter Array or a large South Pole telescope, will change that. The study of the ISM in these objects will vastly benefit from large submillimeter telescopes, array receivers, and millimeter/submillimeter interferometers located south of the equator. Future studies of N159/N160 should include the detailed characterization of the translucent molecular envelope, the dust properties, and the heating and cooling balance of the ISM near and away from star formation sites. Other observational programs could address the creation of molecular clouds by ram pressure compression, and their disruption by star formation activity.

We wish to thank Thomas M. Bania for his thorough review of the draft of this manuscript, the SEST crew at La Silla for a smooth observing run, and the rest of the AST/RO team for their support. The research of A.D.B., J.M.J., and X.Z. was supported in part by the National Science Foundation under a cooperative agreement with the Center for Astrophysical Research in Antarctica (CARA), grant number NSF OPP 89-20223. CARA is a National Science Foundation Science and Technology Center. The research of A.D.B. and J.M.J. was also supported in part by the National Science Foundation through

grant AST-9803065. This research has made use of NASA's Astrophysics Data System Bibliographic Services, the Los Alamos National Laboratory preprint database, and the Centre de Données astronomiques de Strasbourg databases.

### A. Beam filling ratio for two transitions

For this calculation we will assume spherical clumps of radius  $R$ , immersed in an isotropic UV field. A transition turns optically thick (i.e., its opacity,  $\tau$ , is unity) at a distance  $x$  from the surface of the clump. Therefore the radius of the clump at given transition (i.e., the distance from the center of the clump to the transition's  $\tau = 1$  surface) is  $r = R - x$ . The ratio of beam filling fractions  $\Phi$  in two transition will then be proportional to the ratio of the projected areas

$$\frac{\Phi_2}{\Phi_1} = \left( \frac{R - x_2}{R - x_1} \right)^2 \quad (\text{A1})$$

It can be shown easily that for gas in LTE the ratio of optical depths in the ( $J = 1 \rightarrow 0$ ) and ( $J = 2 \rightarrow 1$ ) transitions will be

$$\frac{\tau_{21}}{\tau_{10}} = 2 \frac{\left( 1 - e^{-\frac{h\nu_{21}}{kT_{ex}}} \right)}{\left( e^{\frac{h\nu_{10}}{kT_{ex}}} - 1 \right)} \quad (\text{A2})$$

where  $h$  and  $k$  are Planck's and Boltzmann's constants respectively, and  $T_{ex}$  is the excitation temperature. For uniform density clumps the  $\tau = 1$  surface occurs first for the transition with faster growing opacity, that is,  $x_2/x_1 = \tau_1/\tau_2$ . Equation A1 thus has the solution

$$R = x_1 \frac{\sqrt{\frac{\Phi_2}{\Phi_1}} - \frac{\tau_1}{\tau_2}}{\sqrt{\frac{\Phi_2}{\Phi_1}} - 1} \quad (\text{A3})$$

In order to reproduce the CO ( $J = 2 \rightarrow 1$ )/( $J = 1 \rightarrow 0$ ) intensity ratios observed in regions R1 and R2,  $\Phi_2/\Phi_1 \simeq 3$ . Using  $\tau_2/\tau_1 \simeq 3$  (i.e.,  $T_{ex} \sim 40$  K according to Eq. A2) yields  $R \sim 1.9 x_1$ . Thus  $\tau(1 \rightarrow 0) \sim 2$  at the center of the clump. The average over the whole projected spherical clump is  $\sim 30\%$  larger, or  $\tau(1 \rightarrow 0) \sim 2.5$ .

## REFERENCES

Abgrall, H., Le Bourlot, J., Pineau des Forêts, G., Roueff, E., Flower, D. R., & Heck, L. 1992, A&A, 253, 525

Bolatto, A. D., Jackson, J. M., & Ingalls, J. G. 1999, ApJ, 513, 275

Bolatto, A. D., Jackson, J. M., Wilson, C. D., & Moriarty-Schieven, G. 2000, ApJ, 532, in print

Bouchet, P., Lequeux, J., Maurice, E., Prévot, L., & Prévot-Burnichon, M. L. 1995, A&A, 149, 330

Chu, Y.-H., Kennicutt, R. C., Snowden, S. L., Smith, R. C., Williams, R. M., & Bomans, D. J. 1997, PASP, 109, 554

Cioni, M. R., Habing, H. J., & Israel, F. P. 2000, A&A, 358, L9

Cohen R. S., Dame T. M., Garay G., Montani J., Rubio M., & Thaddeus P. 1988, ApJ, 331, L95

Comerón, F., & Claes, P. 1998, A&A, 335, L13

Cowley, A. P., Schmidtke, P. C., Anderson, A. L., McGrath, T. K. 1995, PASP, 107, 145

Davies, R. D., Elliot, K. H., & Meaburn, J. 1976, MmRAS, 81, 89

de Boer, K. S., Braun, J. M., Vallenari, A., & Mebold, U. 1998, A&A, 329, L49

Dufour, R. J. 1984, in Structure and Evolution of the Magellanic Clouds, ed. S. van der Bergh & K. S. de Boer (Dordrecht:Kluwer), 353

Franco, J., & Cox, D. P. 1986, PASP, 98, 1076

Gerin, M., & Phillips, T. G. 2000, ApJ, in print

Habing, H. J. 1967, Bull. Astron. Inst. Netherlands, 19, 421

Heikkilä, A., Johansson, L. E. B., & Olofsson, H. 1999, A&A, 344, 817

Henize, K. G. 1956, ApJS, 2, 315

Ingalls, J. G., Chamberlin, R. A., Bania, T. M., Jackson, J. M., Lane, A. P., & Stark, A. A. 1997, ApJ, 479, 296

Israel, F.P. et al. 1993, A&A, 276, 25

Israel, F. P., Maloney, P. R., Geis, N., Hermann, F., Madden, S.C., Poglitsch, A., & Stacey, G. J. 1996, ApJ, 465, 738

Israel, F. P. 1997, A&A, 328, 471

Jackson, J. M., & Kraemer, K. E. 1999, ApJ, 512, 250

Johansson, L. E. B., Olofsson, H., Hjalmarson, Å., Gredel, R., & Black, J. H. 1994, A&A, 292, 371

Johansson, L. E. B., et al. 1998, A&A, 331, 857

Kaufman, M. J., Wolfire, M. G., Hollenbach, D. J., & Luhman, M. L. 1999, ApJ, 527, 795

Kim, S., Staveley-Smith, L., Dopita, M. A., Freeman, K. C., Sault, R. J., Kesteven, M. J., & McConnell, D. 1998, ApJ, 503, 674

Koornneef, J. 1982, A&A, 107, 247

Kutner, M. L., et al. 1997, A&AS, 122, 255

Lequeux, J., Peimbert, M., Rayo, J. F., Serrano, A., & Torres-Peimbert, S. 1979, A&A, 80, 155

Lepp, S., & Dalgarno, A. 1996, A&A, 306, L21

Lisenfeld, U., & Ferrara, A. 1998, ApJ, 496, 145

Madden, S. C., Poglitsch, A., Geis, N., Stacey, G. J., & Townes, C. H. 1997, ApJ, 483, 200

Mathewson, D. S., & Ford, V. L. 1984, in Structure and Evolution of the Magellanic Clouds, ed. S. van den Bergh & K. S. de Boer (Dordrecht:Reidel), 125

Meixner, M., & Tielens, A. G. G. M. 1993, ApJ, 405, 216

Meixner, M., & Tielens, A. G. G. M. 1995, ApJ, 446, 907

Mochizuki, K. et al. 1994, ApJ, 430, L37

Pak, S., Jaffe, D. T., van Dishoeck, E. F., Johansson, L. E. B., & Booth, R. S. 1998, ApJ, 498, 735

Panagia, N. 1973, AJ, 78, 929

Panagia, N., Gilmozzi, R., & Kirshner, R. P. 1997, in ASP Conf. Ser., SN 1987A: Ten Years After, ed. M. Phillips & N. Suntzeff (San Francisco:ASP), in print

Poglitsch, A., Krabbe, A., Madden, S. C., Nikola, T., Geis, N., Johansson, L. E. B., Stacey, G. J., & Sternberg, A. 1995, ApJ, 454, 293

Rubio, M., Lequeux, J., & Boulanger, F. 1993, A&A, 271, 9

Schmidtke, P. C., Ponder, A. L., & Cowley, A. P. 1999, AJ, 117, 1292

Spitzer, L. 1978, Physical Processes in the Interstellar Medium (New York:John Wiley & Sons), 47

Stark, A. A., Bolatto, A. D., Chamberlin, R. A., Lane, A. P., Bania, T. M., Jackson, J. M., & Lo, K.-Y. 1997a, ApJ, 480, L59

Stark, A. A., Chamberlin, R. A., Cheng, J., Ingalls, J. G., & Wright, G. 1997b, Rev. Sci. Inst., 68 (5), 2200

Warin, S., Benayoun, J. J., & Viala, Y. P. 1996, A&A, 308, 535

Wilson, C. D. 1997, ApJ, 487, L49

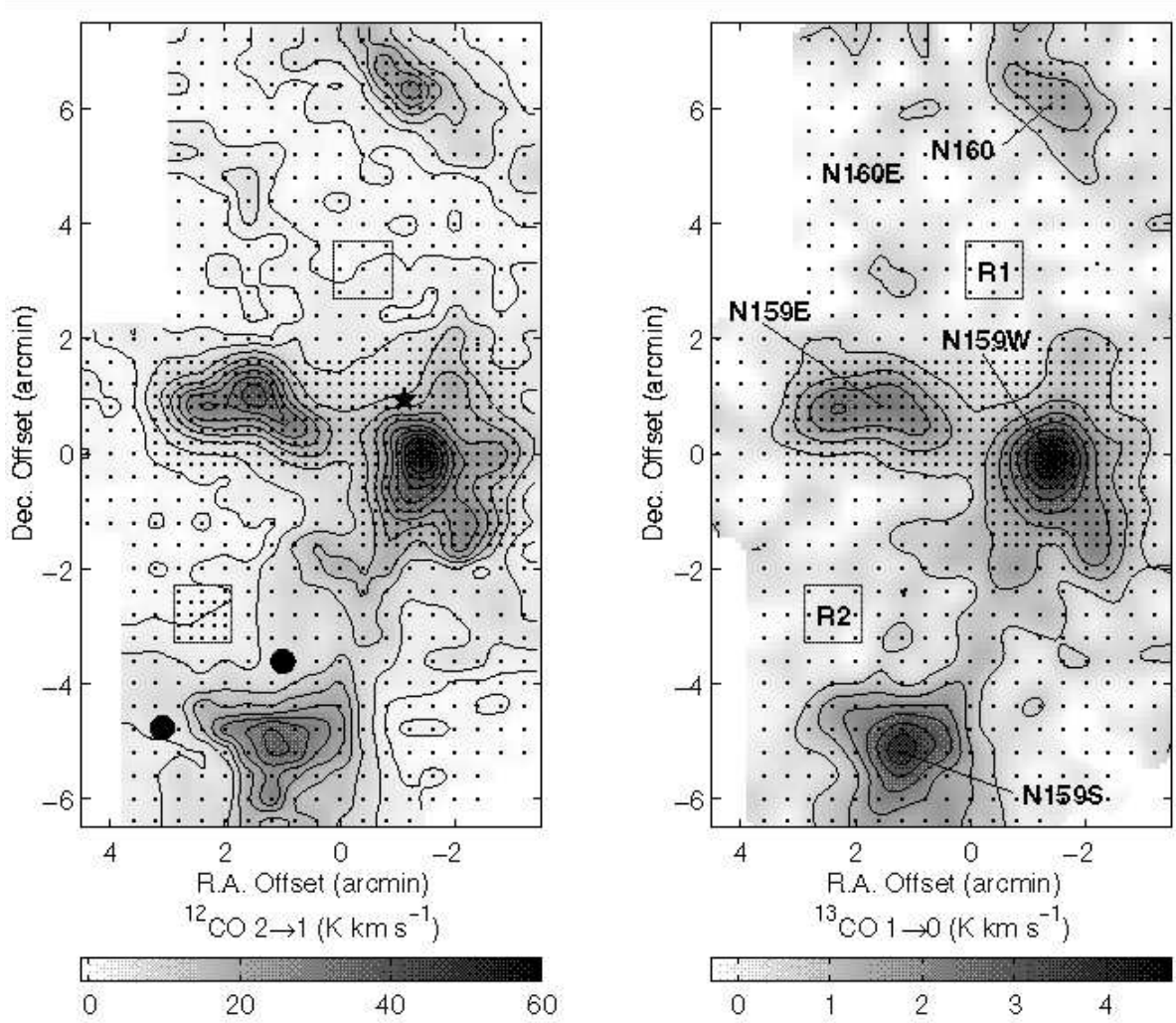


Fig. 1.— Carbon monoxide main beam integrated intensity maps acquired at SEST. The  $^{12}\text{CO}$  ( $J = 2 \rightarrow 1$ ) contours (left panel) are 2, 5, 10, 15, ..., 55  $\text{K km s}^{-1}$  ( $\sigma_{rms} \sim 0.6 \text{ K km s}^{-1}$ ) and the data have been convolved with a Gaussian profile to  $33''$  resolution. The  $^{13}\text{CO}$  ( $J = 1 \rightarrow 0$ ) contours (right panel) are 0.6 to 4.4 at 0.6  $\text{K km s}^{-1}$  intervals ( $\sigma_{rms} \sim 0.2 \text{ K km s}^{-1}$ ) and the map has been convolved to  $60''$  resolution. The individual pointing locations are shown by small dots. The boxes show the position of the two regions with low level extended emission also observed in  $^{12}\text{CO}$  ( $J = 1 \rightarrow 0$ ). The map intensities have been integrated over the velocity range 225 to 245  $\text{km s}^{-1}$ . The black star denotes the position of the black-hole candidate and strong X-ray source LMC-X1. The black circles mark the positions of DEM L272 and L279, the two H II regions closest to N159S. The  $^{13}\text{CO}$  ( $J = 1 \rightarrow 0$ ) map has been annotated with the nomenclature used in Table 1.

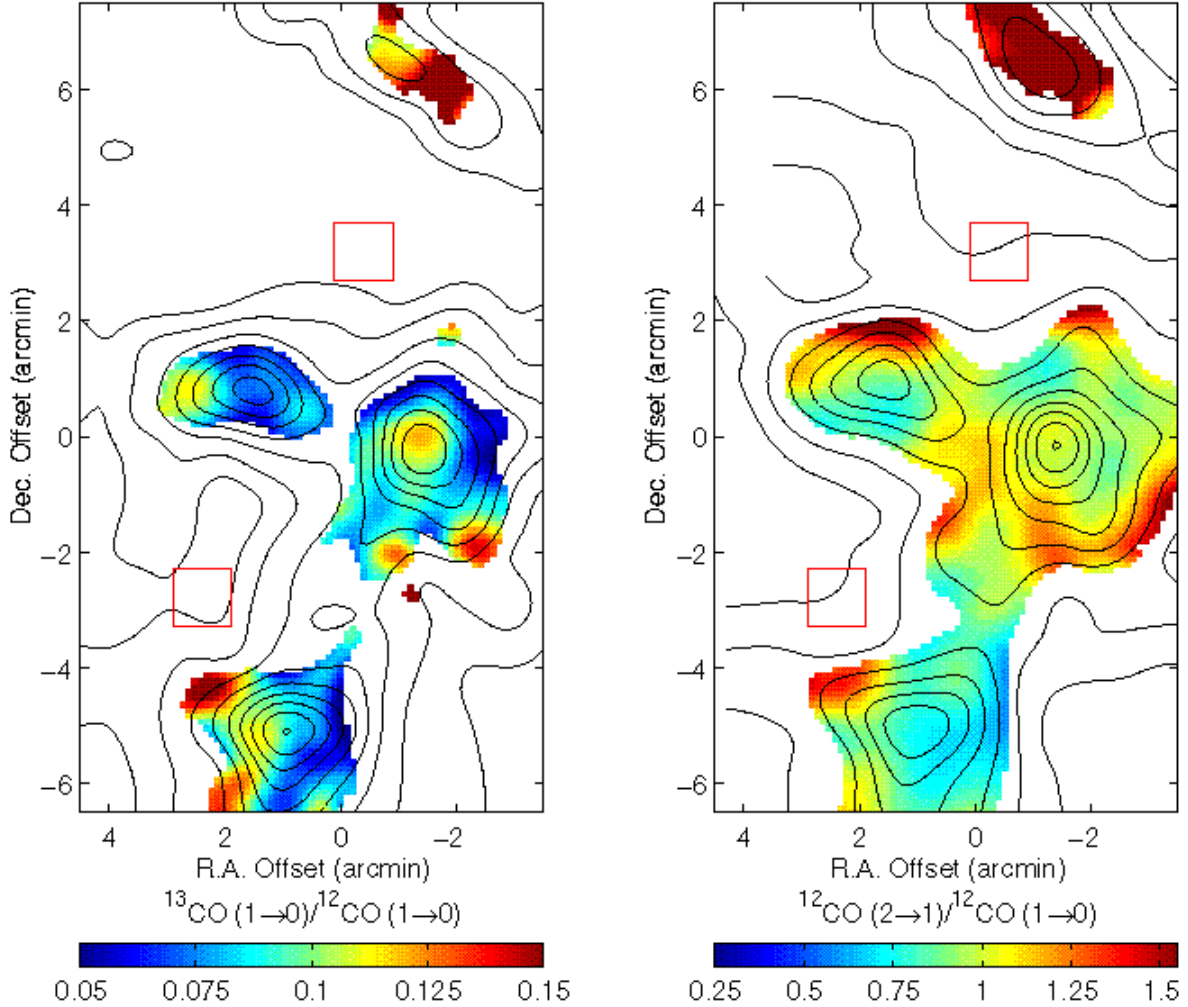


Fig. 2.— Comparison of  $^{12}\text{CO}$  ( $J = 2 \rightarrow 1$ ) and  $^{13}\text{CO}$  ( $J = 1 \rightarrow 0$ ) emission with published  $^{12}\text{CO}$  ( $J = 1 \rightarrow 0$ ) data (Johansson et al. 1998). All maps have been Gaussian smoothed to a common resolution of  $60''$ . The contour levels are the same in both maps (2, 5, 10, 15, ..., 40 K km s $^{-1}$ ). Note that the  $^{12}\text{CO}$  ( $J = 1 \rightarrow 0$ ) map was acquired by frequency switching, and required an elaborate baseline subtraction scheme. Therefore the lowest contour is very unreliable. (Left) Main beam integrated intensity  $^{12}\text{CO}$  ( $J = 1 \rightarrow 0$ ) contour data (Johansson et al. 1998) overlaid on the  $^{13}\text{CO}/^{12}\text{CO}$  ( $J = 1 \rightarrow 0$ ) ratio image. Blue denotes low  $^{13}\text{CO}/^{12}\text{CO}$  ratios and therefore optically thinner CO emission, whereas red shows high ratios and optically thicker emission. (Right) Main beam integrated intensity  $^{12}\text{CO}$  ( $J = 2 \rightarrow 1$ ) contour data overlaid on the  $^{12}\text{CO}$  ( $J = 2 \rightarrow 1$ )/( $J = 1 \rightarrow 0$ ) ratio image. Blue signifies low ( $J = 2 \rightarrow 1$ )/( $J = 1 \rightarrow 0$ ) ratios, and therefore possibly cooler (less dense) gas; red zones are warmer (denser).

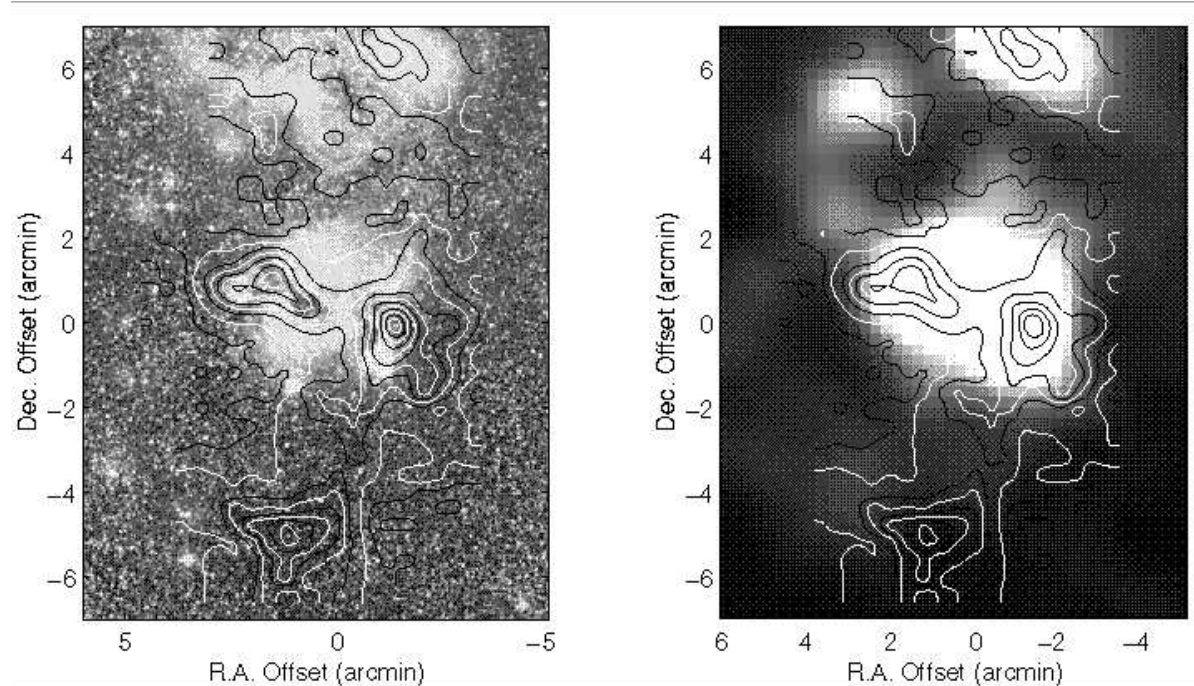


Fig. 3.— Heating of the molecular cloud complex. The optical (left panel, blue band, SERC) and 60  $\mu\text{m}$  FIR (right panel, IRAS HIRES, 40 iterations) emission are shown here with  $^{12}\text{CO}$  ( $J = 2 \rightarrow 1$ ) contours overlaid (alternate black and white, same levels as Fig. 1). This picture illustrates the detailed structure of the nebulae and the intimate and complex association between nebulosity, obscuration lanes, and molecular clumps. The southern cloud appears to have no UV or heating sources associated with it.

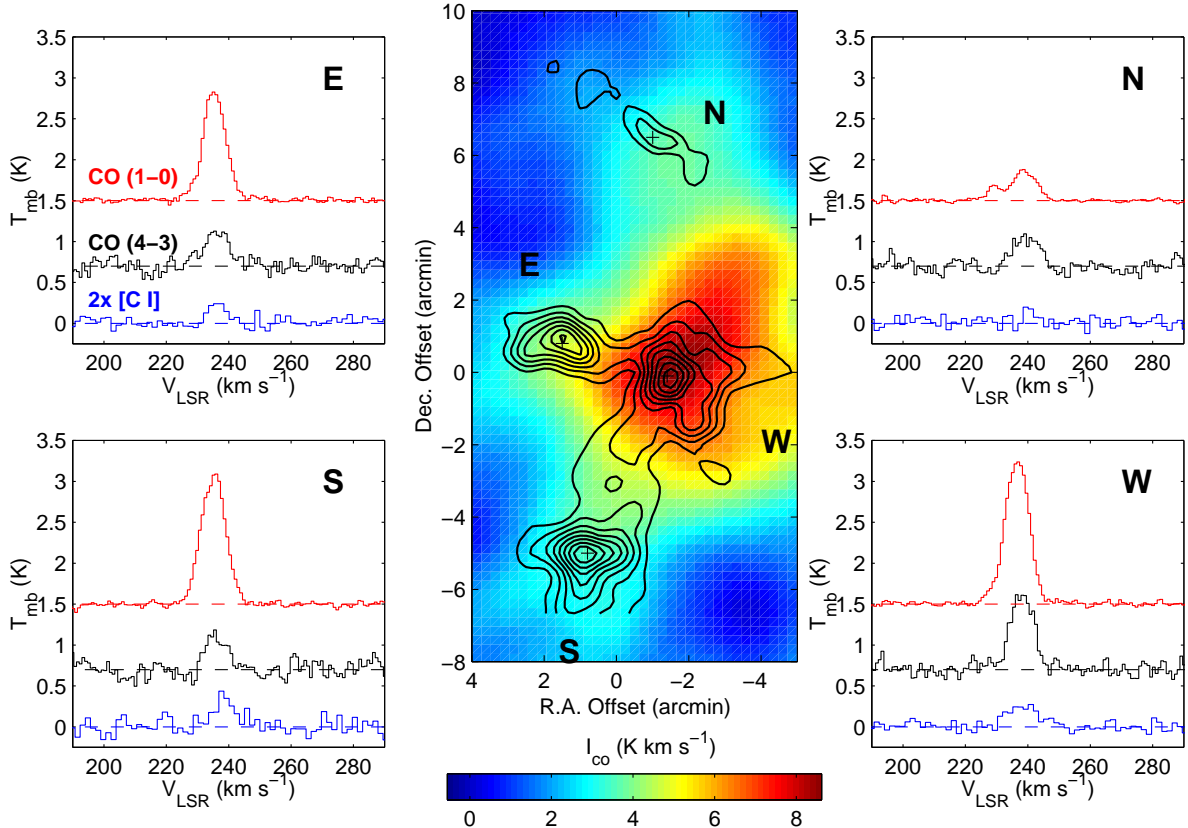


Fig. 4.— Color image of the  $^{12}\text{CO}$  ( $J = 4 \rightarrow 3$ ) integrated intensity map with  $^{12}\text{CO}$  ( $J = 1 \rightarrow 0$ ) data overlaid. The ( $J = 4 \rightarrow 3$ ) data has been smoothed to a  $4'$  spatial resolution. Marked by crosses are the positions of the four main molecular peaks in the region. Their corresponding  $^{12}\text{CO}$  ( $J = 4 \rightarrow 3$ ) (black) and  $[\text{C I}]$  (blue) spectra are shown on the side (the  $[\text{C I}]$  spectra have been scaled up by a factor of two) For purposes of comparison, shown in red are the  $^{12}\text{CO}$  ( $J = 1 \rightarrow 0$ ) spectra (Johansson et al. 1998) convolved to the same angular resolution ( $4'$  HPBW). The relative enhancement and deficit of ( $J = 4 \rightarrow 3$ ) in the N160 (labeled N) and N159S (labeled S) clouds respectively are apparent.

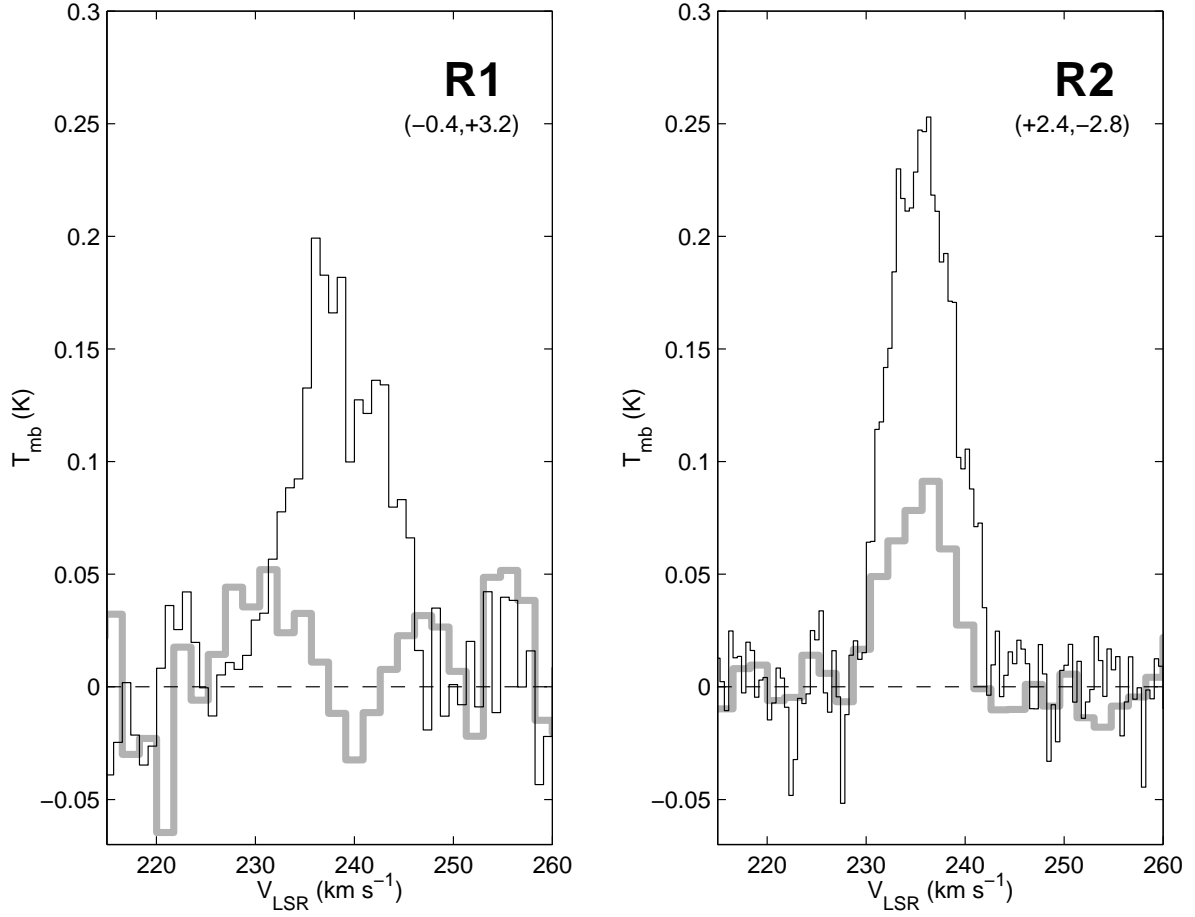


Fig. 5.— Observed spectra of the  $^{12}\text{CO}(J = 1 \rightarrow 0)$  and  $(J = 2 \rightarrow 1)$  transitions for the faint extended molecular emission. These two regions are identified here by their offsets and drawn on Fig. 1. The  $(J = 2 \rightarrow 1)$  transition (fine black line) produces the strongest lines in both regions while the  $(J = 1 \rightarrow 0)$  (wide gray line) is weaker by a factor  $\gtrsim 3$ , suggesting optically thin emission.

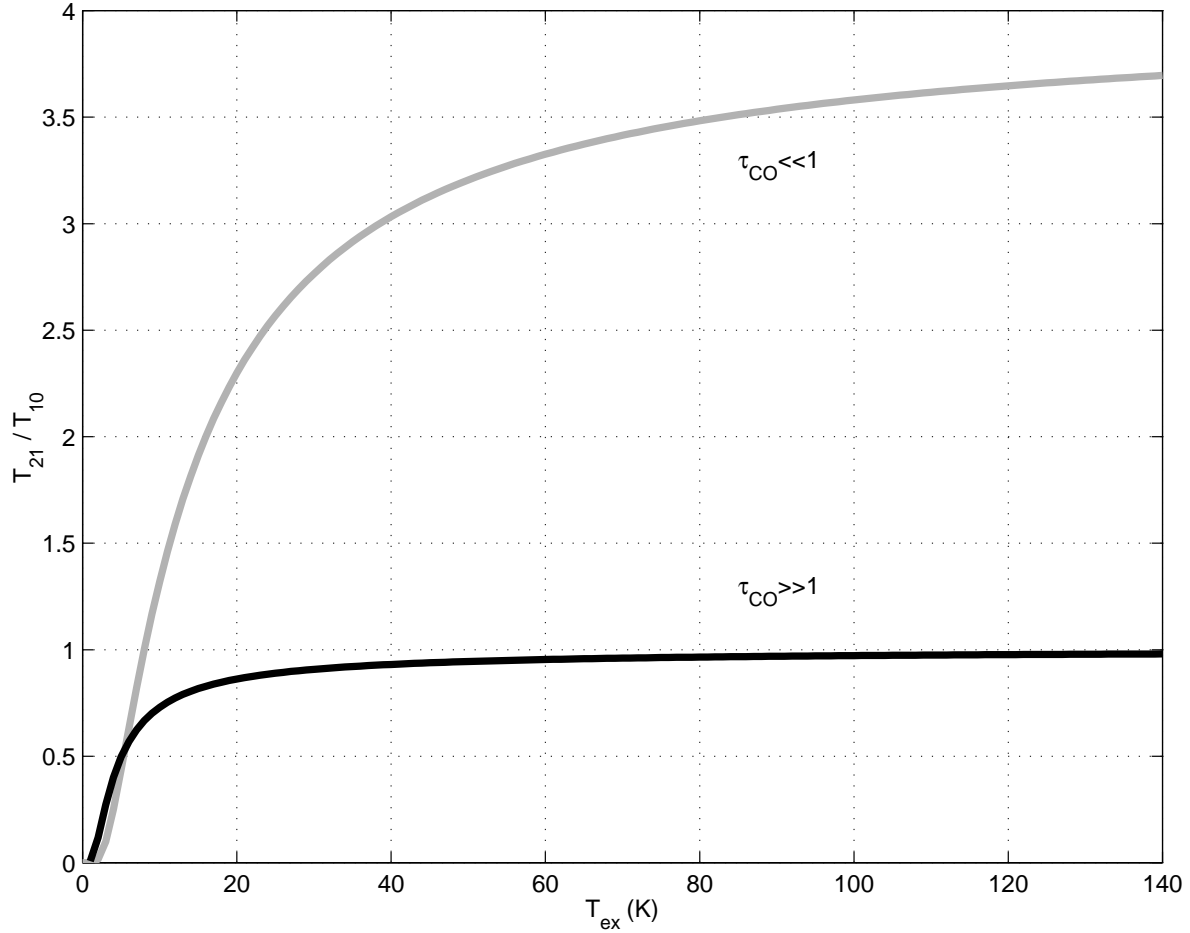


Fig. 6.— Ratio of ( $J = 2 \rightarrow 1$ ) to ( $J = 1 \rightarrow 0$ ) integrated brightness temperature for CO emission in local thermodynamic equilibrium (LTE), as a function of the excitation temperature  $T_{ex}$ . The black line corresponds to optically thick emission. The grey line is the plot of Eq. 1 for  $n = 1$ , valid under optically thin conditions.

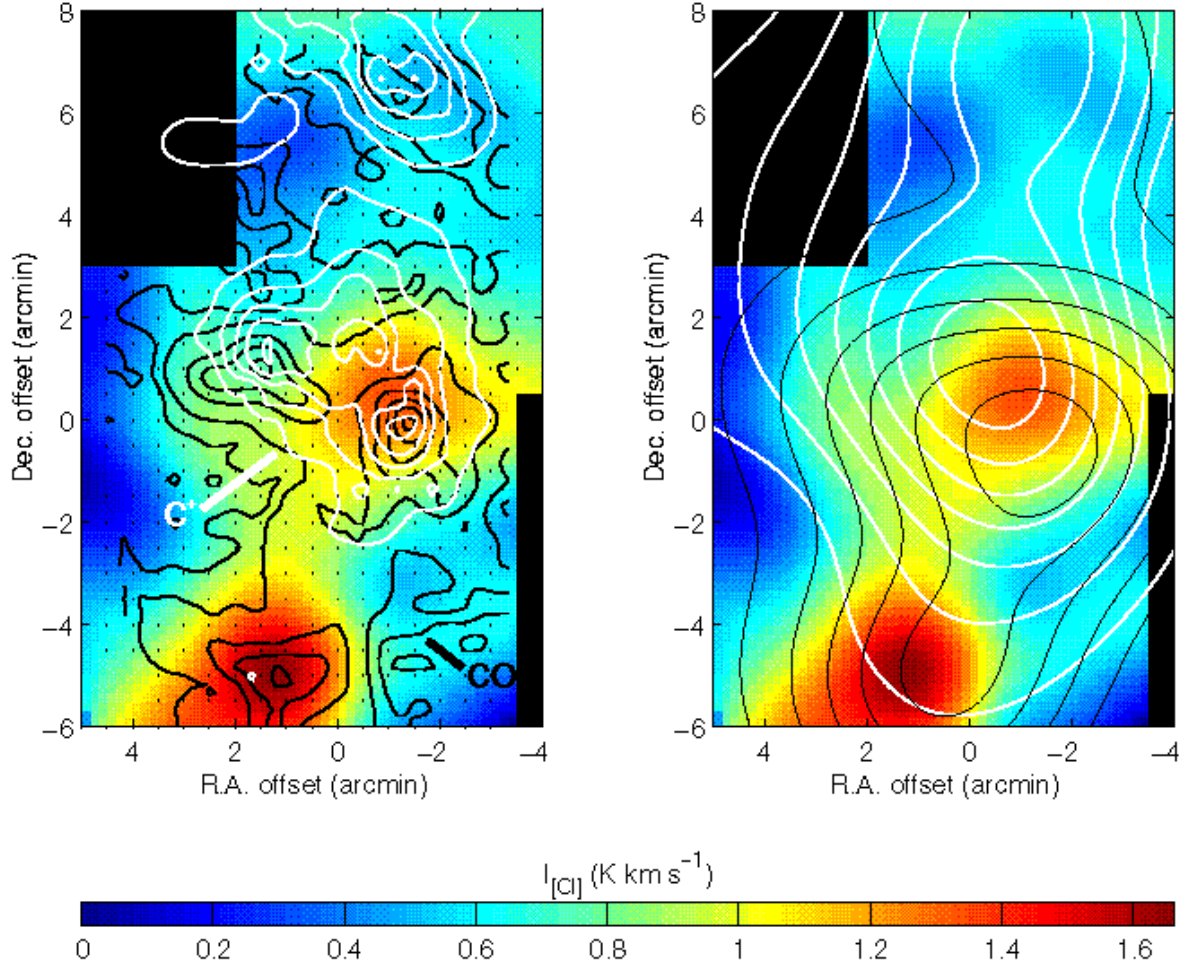


Fig. 7.— Distribution of the three dominant forms of gas phase carbon in N159/N160. The pseudo color image shows the AST/RO [C I] observations at an angular resolution of  $\sim 4.3'$  (sensitivity  $1\sigma \sim 0.1 \text{ K km s}^{-1}$ ). (Left) In black contours is the CO ( $J = 2 \rightarrow 1$ ) map, at a resolution  $\sim 33''$  (contours 2,5,15,25,...,55  $\text{K km s}^{-1}$ ). In white contours is the [C II] map by Israel et al. (1996), at a resolution  $\sim 55''$  (contours start at  $6.8 \times 10^{-5}$  in steps of  $6.8 \times 10^{-5} \text{ erg s}^{-1} \text{ cm}^{-2} \text{ sr}^{-1}$ ). (Right) The three transitions have been smoothed to a common resolution of  $4.3'$ . We use here the CO ( $J = 1 \rightarrow 0$ ) map by Johansson et al. (1994) to avoid edge effects when convolving the CO. The CO intensity contours start at 2  $\text{K km s}^{-1}$  in steps of 2  $\text{K km s}^{-1}$ . The  $I_{[\text{CII}]}$  contours start at  $1 \times 10^{-5}$  in steps of  $2 \times 10^{-5} \text{ erg s}^{-1} \text{ cm}^{-2} \text{ sr}^{-1}$ .

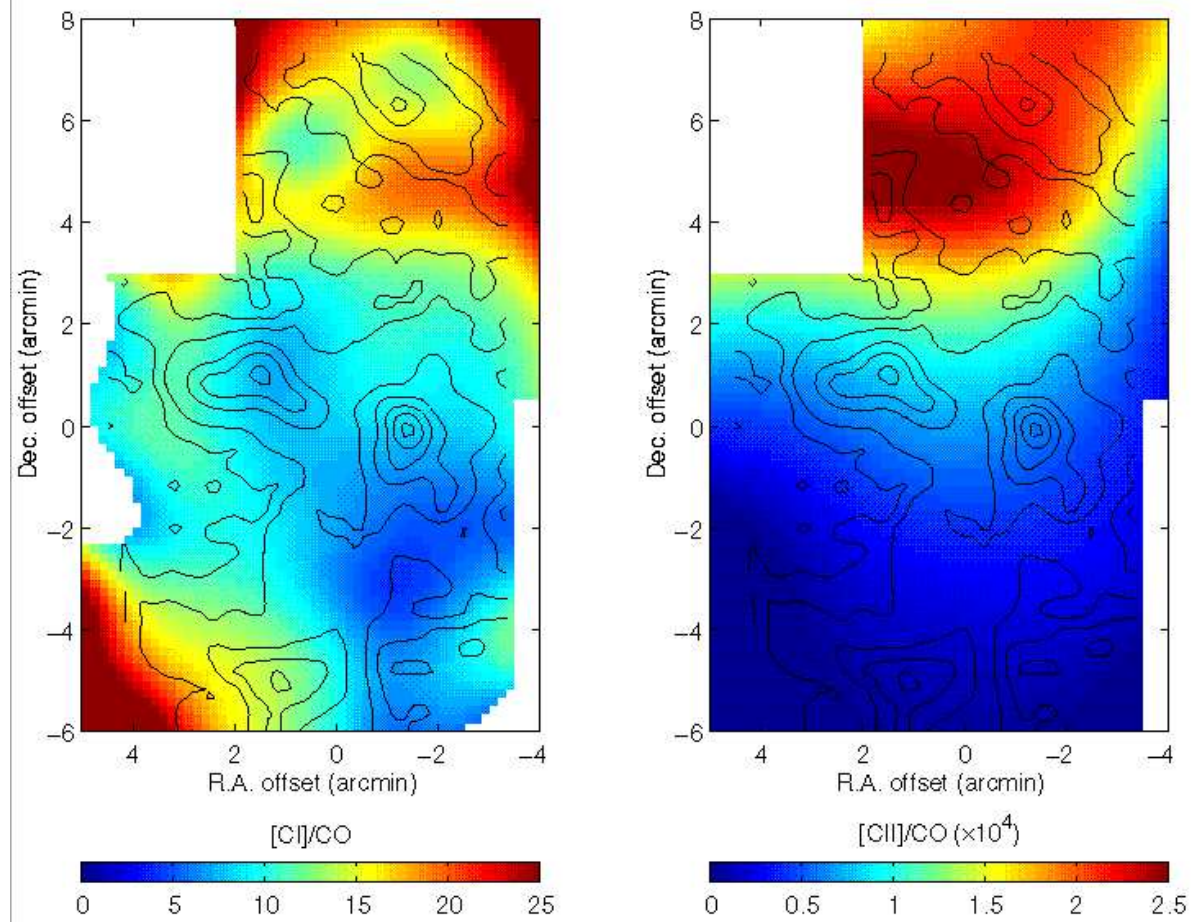


Fig. 8.— Maps of the  $I_{\text{[CII]}}/I_{\text{CO}}$  and  $I_{\text{[CIII]}}/I_{\text{CO}}$  ratios throughout the N159/N160 complex. (Left) Image of the  $I_{\text{[CII]}}/I_{\text{CO}}$  integrated intensity ratio, with  $I_{\text{[CII]}}$  and  $I_{\text{CO}}$  ( $J = 1 \rightarrow 0$ ) in  $\text{erg s}^{-1} \text{cm}^{-2} \text{sr}^{-1}$ . The CO ( $J = 2 \rightarrow 1$ ) contours are overlaid to serve as a reference, but the ( $J = 1 \rightarrow 0$ ) map from Johansson et al. (1994) was used to produce the ratio, thereby eliminating edge problems in the CO dataset. (Right) Image of the  $I_{\text{[CIII]}}/I_{\text{CO}}$  integrated intensity ratio. Typical Galactic ratios are  $I_{\text{[CII]}}/I_{\text{CO}} \sim 10$  and  $I_{\text{[CIII]}}/I_{\text{CO}} \sim 4400$ . All maps have been convolved to the same  $\sim 4.3'$  angular resolution.

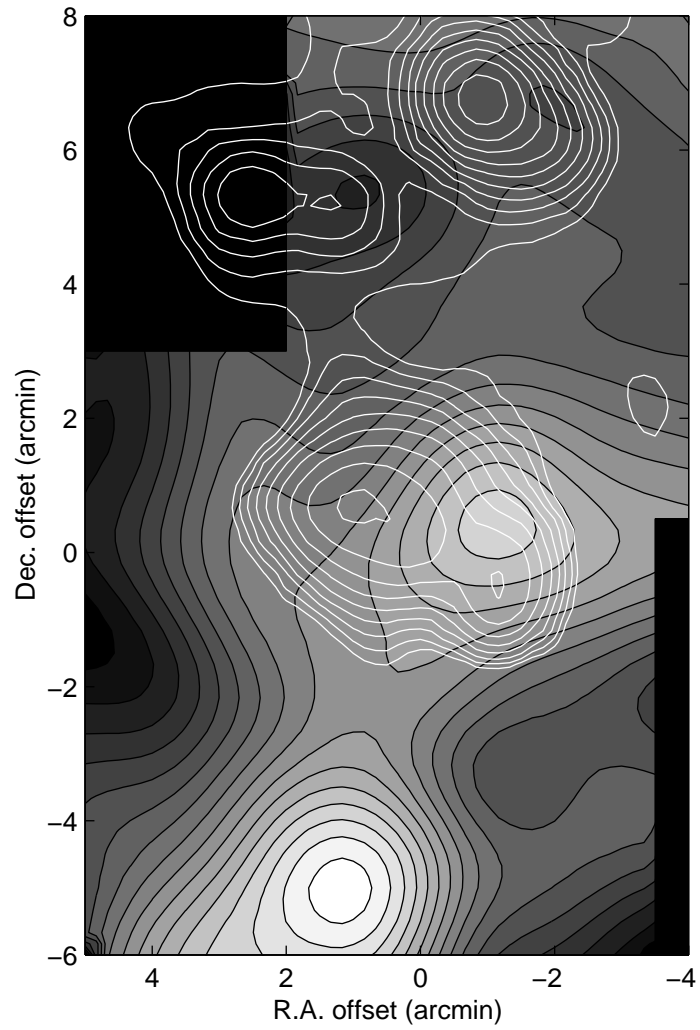


Fig. 9.— Maps of neutral carbon emission and 21 cm radio continuum. The radio continuum contours (white) start at 30 mJy and are logarithmically spaced by a factor of 1.4. The highest contour is at 620 mJy. The  $I_{[CI]}$  contours (grayscale) start at 0 K km s<sup>-1</sup> and go to 1.6 in steps of 0.1 K km s<sup>-1</sup>.

Table 1. Positions and Properties of the Regions of Interest in N159/N160

Identifier	R.A. (B 1950)	Dec. (B 1950)	R.A. offset (arcmin)	Dec. offset (arcmin)	$n(\text{H}_2)$ <sup>a</sup> (cm <sup>-3</sup> )	$N_{\text{H}_2}$ <sup>a,d</sup> (cm <sup>-2</sup> )	$\chi_{uv}$ <sup>b,c</sup>	$I_{[\text{CII}]}/I_{\text{CO}}$ <sup>b</sup>
N159W	5 <sup>h</sup> 40 <sup>m</sup> 02 <sup>s</sup> .2	−69°47'06"	−1.4	−0.1	$3 \times 10^5$	$1.1 \times 10^{22}$	600—250	5600
N159E	5 <sup>h</sup> 40 <sup>m</sup> 35 <sup>s</sup> .8	−69°46'12"	+1.5	+0.8	...	...	...	13000
N159S	5 <sup>h</sup> 40 <sup>m</sup> 27 <sup>s</sup> .7	−69°52'00"	+0.8	−5.0	$1 \times 10^5$	$1.7 \times 10^{22}$	60—6	400
N160	5 <sup>h</sup> 40 <sup>m</sup> 06 <sup>s</sup> .9	−69°40'30"	−1.0	+6.5	$5 \times 10^5$	$1.1 \times 10^{22}$	450—200	34000
N160E	5 <sup>h</sup> 40 <sup>m</sup> 46 <sup>s</sup> .1	−69°41'48"	+2.8	+5.2	...	...	...	...
R1	5 <sup>h</sup> 40 <sup>m</sup> 13 <sup>s</sup> .8	−69°43'48"	−0.4	+3.2	...	$6 \times 10^{20}$	200—50	...
R2	5 <sup>h</sup> 40 <sup>m</sup> 46 <sup>s</sup> .2	−69°49'48"	+2.4	−2.8	...	$2—6 \times 10^{20}$	100—10	...

<sup>a</sup>From the mm multiline excitation analysis by Heikkilä et al. (1999).

<sup>b</sup>From Israel et al. (1996).

<sup>c</sup>From this work.

<sup>d</sup>To convert to visual extinction,  $A_V$ , divide by  $4 \times 10^{21}$ .

Table 2. Measured Millimeter Line Parameters in N159/N160

Identifier	$T_{mb}$ <sup>a,b</sup> (K)	$V_{LSR}$ <sup>b</sup> (km s <sup>-1</sup> )	FWHM <sup>b</sup> (km s <sup>-1</sup> )	$I = \int T_{mb} dv$ <sup>a</sup> (K km s <sup>-1</sup> )	$I/I_{10}$ <sup>c,d</sup>
<sup>e</sup>					
<sup>13</sup> CO ( $J = 1 \rightarrow 0$ )					
N159W	0.64±0.01	238.1±0.1	6.9±0.1	4.67±0.04	0.12±0.02
N159E	0.60±0.01	234.6±0.1	6.1±0.1	2.13±0.04	0.07±0.01
N159S	0.57±0.01	235.6±0.1	5.7±0.1	3.37±0.07	0.10±0.01
N160	0.56±0.01	237.7±0.1	4.6±0.2	1.39±0.06	0.12±0.02
R1	...	...	...	0.01±0.10	...
R2	...	...	...	0.09±0.11	...
<sup>e</sup>					
<sup>12</sup> CO ( $J = 2 \rightarrow 1$ )					
N159W	4.80±0.01	237.7±0.1	7.8±0.1	39.12±0.06	1.01±0.14
N159E	3.60±0.01	234.6±0.1	7.3±0.1	27.42±0.06	0.89±0.13
N159S	3.22±0.01	234.9±0.1	8.1±0.1	27.00±0.08	0.78±0.11
N160	3.46±0.01	237.7±0.1	5.0±0.1	18.24±0.10	1.59±0.23
R1	0.16±0.01	238.0±0.7	10.8±1.5	1.75±0.20	3.57±1.40
R2	0.25±0.01	235.4±0.2	7.6±0.4	1.94±0.10	2.81±0.64

<sup>a</sup>Errors are statistical and  $\pm 1\sigma$ . Systematic calibration uncertainty is  $1\sigma \sim \pm 10\%$ .

<sup>b</sup>Values and errors derived from Gaussian fit.

<sup>c</sup>Ratio of transition intensity to that of  $^{12}\text{CO}(J = 1 \rightarrow 0)$ , convolved to the same beam, in K km s<sup>-1</sup>.

<sup>d</sup>Errors are  $\pm 1\sigma$ , and include 10%  $1\sigma$  calibration uncertainty in both lines.

<sup>e</sup>Measured in a HPBW=1' beam.

Table 3. Measured Submillimeter Line Parameters in N159/N160

Identifier	$T_{mb}$ <sup>a,b</sup> (K)	$V_{LSR}$ <sup>b</sup> (km s <sup>-1</sup> )	FWHM <sup>b</sup> (km s <sup>-1</sup> )	$I = \int T_{mb} dv$ <sup>a</sup> (K km s <sup>-1</sup> )	$I/I_{10}$ <sup>c,d</sup>	$I_{[CII]}/I_{CO}$ <sup>e</sup>
<sup>f</sup>						
<sup>12</sup> CO ( $J = 4 \rightarrow 3$ )	0.95±0.01	237.7±0.1	8.6±0.1	8.43±0.08	0.58±0.09	
N159W	0.42±0.01	235.6±0.1	10.2±0.2	4.42±0.09	0.48±0.07	
N159E	0.40±0.01	235.5±0.1	7.7±0.2	3.41±0.08	0.27±0.04	
N160	0.39±0.07	239.1±0.1	9.4±0.2	3.81±0.08	1.16±0.17	
C <sup>0</sup> ( ${}^3P_1 \rightarrow {}^3P_0$ )						
N159W	0.13±0.01	237.6±0.1	11.8±0.4	1.59±0.05	0.11±0.02	6000
N159E	0.14±0.01	235.5±0.1	6.1±0.3	0.87±0.03	0.09±0.01	7900
N159S	0.17±0.01	238.1±0.1	10.1±0.4	1.90±0.06	0.15±0.02	1000
N160	0.14±0.01	239.2±0.1	2.4±0.1	0.34±0.02	0.10±0.02	21700
R1	0.06±0.01	238.3±0.3	9.1±0.7	0.55±0.04	0.14±0.02	17800
R2	0.09±0.01	236.6±0.2	7.7±0.6	0.73±0.05	0.12±0.02	1700

<sup>a</sup>Errors are statistical and  $\pm 1\sigma$ . Systematic calibration uncertainty is  $1\sigma \sim \pm 10\%$ .

<sup>b</sup>Values and errors derived from Gaussian fit.

<sup>c</sup>Ratio of transition intensity to that of  ${}^{12}\text{CO}(J = 1 \rightarrow 0)$ , convolved to the same beam, in K km s<sup>-1</sup>. To obtain ratios for intensities in erg s<sup>-1</sup> cm<sup>-2</sup> sr<sup>-1</sup> multiply by  $(\nu/\nu_{10})^3$ .

<sup>d</sup>Errors are  $\pm 1\sigma$ , and include 10%  $1\sigma$  calibration uncertainty in both lines.

<sup>e</sup>[CII]/CO ( $J = 1 \rightarrow 0$ ) line intensity ratio in a 4' beam, in erg s<sup>-1</sup> cm<sup>-2</sup> sr<sup>-1</sup>.

<sup>f</sup>Measured in a HPBW=4' beam.

Table 4. FIR Parameters for the N159/N160 Complex

Identifier	$S_{60}$ <sup>a</sup> (Jy)	$S_{100}$ <sup>a</sup> (Jy)	$\frac{S_{100}}{S_{60}}$	$T_{dust}$ <sup>b</sup> (K)	$L_{FIR}$ <sup>c</sup> ( $10^6 L_{\odot}$ )	Eq. Sp. Type <sup>d</sup> (ZAMS)
N159W	204.9	671.8	3.28	30	3.40	5×O5V
N159E	179.6	393.7	2.19	34	1.86	3×O5V
N159S <sup>e</sup>	6.6	39.5	6.01	25	< 0.24	<O6V
N160	393.1	580.1	1.48	40	2.74	4×O5V
N160E	48.5	76.1	1.57	39	0.36	O5.5V

<sup>a</sup>Point source flux density at 60 and 100  $\mu$ m derived from IRAS HIRES data.

<sup>b</sup>Dust temperature derived from the ratio of  $S_{100}$  to  $S_{60}$ , assuming the dust emits as a graybody with emissivity exponent  $\beta = 1$ .

<sup>c</sup>FIR luminosity computed according to Lonsdale (1985), assuming a dust emissivity exponent  $\beta = 1$  and  $D = 52$  kpc.

<sup>d</sup>Equivalent spectral type and multiplicity (Panagia 1973), assuming all starlight is absorbed by dust and reemitted in the FIR.

<sup>e</sup>There is no infrared source associated with N159S, therefore the IRAS fluxes are upper limits.

Table 5. Radio Continuum Sources in the N159/N160 Complex

Identifier	R.A. (B1950)	Dec. (B1950)	$S_{1.42}$ <sup>a</sup> (mJy)	$U$ <sup>b</sup> (pc cm <sup>-2</sup> )	Sp. Type <sup>c</sup> (ZAMS)
N159-I	5 <sup>h</sup> 40 <sup>m</sup> 29 <sup>s</sup> .3	-69°46'21"	480	143	1.5×O5V
N159-II	5 <sup>h</sup> 40 <sup>m</sup> 05 <sup>s</sup> .2	-69°47'29"	440	139	1.4×O5V
N159-III	5 <sup>h</sup> 40 <sup>m</sup> 22 <sup>s</sup> .4	-69°46'37"	336	127	1.3×O5V
N159S <sup>d</sup>	...	...	< 30	< 57	<O6V
N160-I	5 <sup>h</sup> 40 <sup>m</sup> 07 <sup>s</sup> .8	-69°40'17"	802	170	1.7×O5V
N160-II	5 <sup>h</sup> 40 <sup>m</sup> 47 <sup>s</sup> .3	-69°41'42"	169	101	O5V
N160-III	5 <sup>h</sup> 40 <sup>m</sup> 35 <sup>s</sup> .1	-69°41'49"	126	92	O5V

<sup>a</sup>Point source flux density at 21 cm.

<sup>b</sup>H II region excitation parameter.

<sup>c</sup>Equivalent spectral type and multiplicity, derived using  $U$  computed by Panagia (1973).

<sup>d</sup>No radio continuum detected down to  $1\sigma \approx 10$  mJy.